Nanoporous Gold Nanoparticles and Arrays for Label-Free Nanoplasmonic Biosensing

Camille G. Artur and Wei-Chuan Shih

1 Introduction

Surface plasmons (SP) are depicted in the classical picture as a fundamental electromagnetic mode of an interface between a metal (or a semi-conductor) and a dielectric medium and involving surface collective electronic oscillations [1]. Surface plasmons were predicted and described more than 60 years ago, however, plasmonics did not form as a sub-field of photonics dealing with the manipulation of light at the nanoscale until more recently. With rapid technological advances in miniaturization, electronics and optical detection, plasmonics has taken off in the past decade and continued to flourish in both fundamental and applied fields [2, 3].

Metallic nanoparticles and nanostructures with dimensions from a few up to several hundred nanometers, support localized surface plasmon resonance (LSPR) that induce enhanced electromagnetic fields localized at the nanoparticle surface when illuminated by light. The LSPR frequency is highly dependent on the geometry but also on the permittivity of the metal itself as well as the surrounding media. Synthesis and fabrication of a large variety of nanostructures, be they in suspension in the liquid phase (metallic colloids) or on planar substrates has

C.G. Artur · W.-C. Shih (✉)
Department of Electrical & Computer Engineering, University of Houston, 4800 Calhoun Rd, Houston, TX 77204, USA
e-mail: wshih@uh.edu

W.-C. Shih
Department of Biomedical Engineering, University of Houston, Houston, TX 77204, USA

W.-C. Shih
Program of Materials Science & Engineering, University of Houston, Houston, TX 77204, USA

W.-C. Shih
Department of Chemistry, University of Houston, Houston, TX 77204, USA

S.-H. Oh et al. (eds.), *Miniature Fluidic Devices for Rapid Biological Detection*, Integrated Analytical Systems, https://doi.org/10.1007/978-3-319-64747-0_2

enabled a variety of applications. On the other hand, rational design of plasmonic nanoparticles has allowed for the tuning of LSPR frequencies from ultraviolet (UV) up to the mid-infrared (MIR) portions of the electromagnetic spectrum [4].

To date, plasmonics has advanced significantly and become a highly multidisciplinary field with the potential for a wide range of technological applications, many of them having led to commercialization. Among many, two prominent directions are enhanced sensing and light manipulation which directly take advantage of the plasmonic field localization. These two applications are particularly relevant to medicine (diagnostics and therapy) and molecular biology [5, 6, 7]. A particularly useful and often adopted sensing mechanism is based on LSPR's sensitivity to local refractive index changes near the metal surface (so-called LSPR spectroscopy), similar to Surface Plasmon Resonance (SPR) sensors which however relies on propagating surface plasmons. Beyond index sensing, the electromagnetic field localization and enhancement near the nanostructures have been demonstrated to have profound impact on a variety of light–matter interactions such as surface-enhanced Raman scattering (SERS), surface-enhanced Infrared Absorption (SEIRA), surface-enhanced fluorescence (SEF), and recently, surface-enhanced near-infrared absorption (SENIRA) [8] Such surface-enhanced spectroscopy techniques have the ability to detect trace amount of analytes and in certain conditions, down to the single-molecule sensitivity [9]. A tremendous amount of effort has been devoted to designing reliable and low-cost plasmonic-based biosensors and translating them eventually into biological and biomedical applications [10].

Plasmonic nanostructures of gold have emerged as an attractive class of nanomaterials because of their corrosion resistance, relative chemical inertness, and ability to bind to a wide range of thiolated ligands and biomolecular species through the metal–S bond. Historically, gold nanospheres were proposed first as plasmon mediated photothermal therapy agent [11] but in vivo applications were limited because their plasmon resonance is near 540 nm where biological tissue is turbid. Thus, various other colloidal nanoparticles have been developed with a primary goal of shifting the resonance into the near-infrared (NIR) or the so-called "diagnostic widow". Many types and shapes have been developed and they all share the same feature: they are all made out of a solid core [12, 13, 14].

One feature LSPR/SPR-based refractive index (RI) sensing and surface-enhanced spectroscopy techniques have in common is the dramatic dependence on the distance between the target molecule and the metallic surface. The LSPR effect is a near-field, i.e., extremely localized, phenomenon and decays rapidly from the surface. The regions where the electromagnetic field is confined and its intensity greatly amplified are often called "hot spots". It is therefore desirable to optimize the sensor performance by increasing the "optically hot" surface-to-volume ratio while keeping hot spots accessible to the target molecules.

Nanoporous gold (NPG) thin films have recently captured intense attention for their large surface area (Fig. 1) and they have been recognized as plasmonic materials with LSPR frequencies exhibiting pore size dependent tunability [15, 16]. The increased total surface area permits NPG to possess a much higher density of

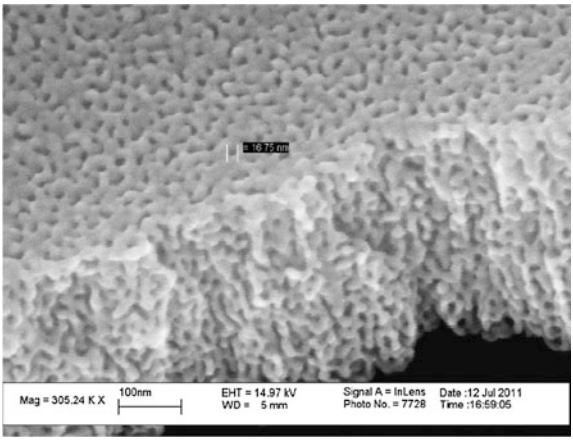

Fig. 1 Nanoporous gold with 300 nm thickness and 15–20 nm pore size from the dellayoing of a gold/silver alloy

potential hot spots for surface adsorbates and NPG thin films are "semi-transparent"; thus even adsorbates over the "internal" surfaces have a chance to be optically measured. Unlike conventional sensors featuring more or less flat sensing surfaces, NPG features an ultrahigh surface-to-volume ratio for collecting a large number of molecules inside the sensing volume.

But NPG films have also some limitations in their use as plasmonic sensor. Their LSPR band centering around 600 nm in an extinction spectrum (far field) has limited tunability of about 50 nm, which is achieved by varying the pore size from 10 to 50 nm [17]. A fundamental reason for the low tunability of NPG thin films is the relatively small pores that are merely a few percent of the optical wavelength. However, since the enhanced electromagnetic fields of LSPR excited in the ligaments are considered a highly desirable feature, a simple idea is to improve coupling between light and plasmons by forming NPG nanoparticles.

In the rest of this chapter, we will discuss the design, fabrication, and characterization of uniform, monolithic NPG nanoparticles produced by the combination of lithographic patterning and dealloying. We will demonstrate that NPG nanoparticles with large surface area, tunable plasmonic resonances, and high-density hot spots. NPG nanoparticles feature a fine porous network with pore size $\sim$20 nm in some embodiments throughout its entire volume; the external shape of the nanoparticles is similar to that of nanodisks whose diameter and thickness can be easily tuned by varying the fabrication parameters. We will show how NPG disks can be integrated into microfluidic devices and will demonstrate their potential as a multifunctional platform for chemical and biological sensing.

Several label-free nanobiosensing applications will be discussed and can be classified in two groups: NPG disks based sensors with or without surface modifications. We will show that the bare-surfaces NPG disks enable quantitative detection of analytes in complex, unprocessed biological fluids such as urine. We will then demonstrate the ultrahigh sensitivity of functionalized NPG disks for sequence-specific DNA hybridization monitoring at the single-molecule level using

molecular sentinel and direct sensing of small molecules such as malachite green using G-quadruplex as a capturing scaffold.

2 Nanoporous Gold Disks Fabrication and Characterization

2.1 Nanosphere Lithography and Dealloying of Au/Ag Films

To fabricate NPG disks, we take advantage of both top-down lithographic patterning and bottom-up atomic dealloying, which together demonstrate great synergy in precisely tuning the plasmonic properties of nanoporous materials. This section describes the fabrication process of the NPG disks (NPGD) substrates whose sensor applications are the core of this chapter [18].

As shown in Fig. 2, a film of gold and silver alloy approximately 120 nm thick was first deposited by DC sputtering onto a substrate (e.g., silicon wafer or glass slide) using an $Ag_{82.5}Au_{17.5}$ (atomic percentages) alloy target. A monolayer of 460–1100 nm diameter polystyrene beads (PS) was then formed on top of the alloy film an coating of over 90% of the alloy surface with close-packed PS beads can be achieved reproducibly [19] (Fig. 2a). Next, a timed oxygen plasma treatment was employed to shrink the PS beads, thus separating them from neighboring beads. The sample was then sputter-etched in argon plasma through the PS mask to transfer the bead pattern into the alloy film (Fig. 2b). Once the pattern transfer was completed, the PS beads were removed by sonication in chloroform or in isopropanol for 30 s (Fig. 2c). The alloy disks were dealloyed in concentrated nitric

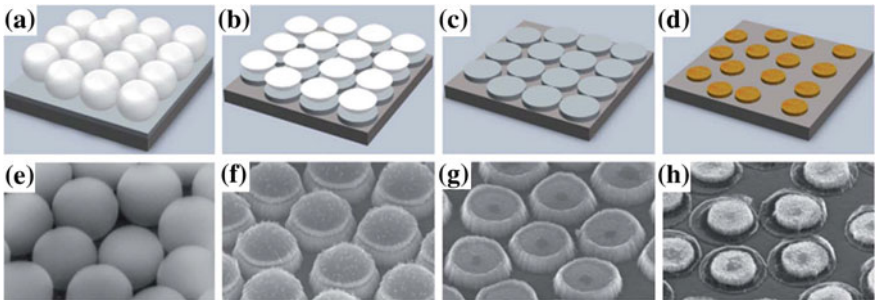

Fig. 2 **a–d** Illustration of the fabrication process used to prepare NPG disks on a silicon (or glass) substrate: (**a**) formation of a monolayer of polystyrene (PS) beads on an alloy-coated silicon (or glass) substrate; (**b**) O_2 plasma shrinkage of the PS beads and Ar sputter etching to form isolated alloy disks; (**c**) selective dissolution of PS beads by chloroform; (**d**) formation of NPG disks by dealloying. Figures (**e–h**) are SEM images taken at each step of the process with a 45° viewing angle

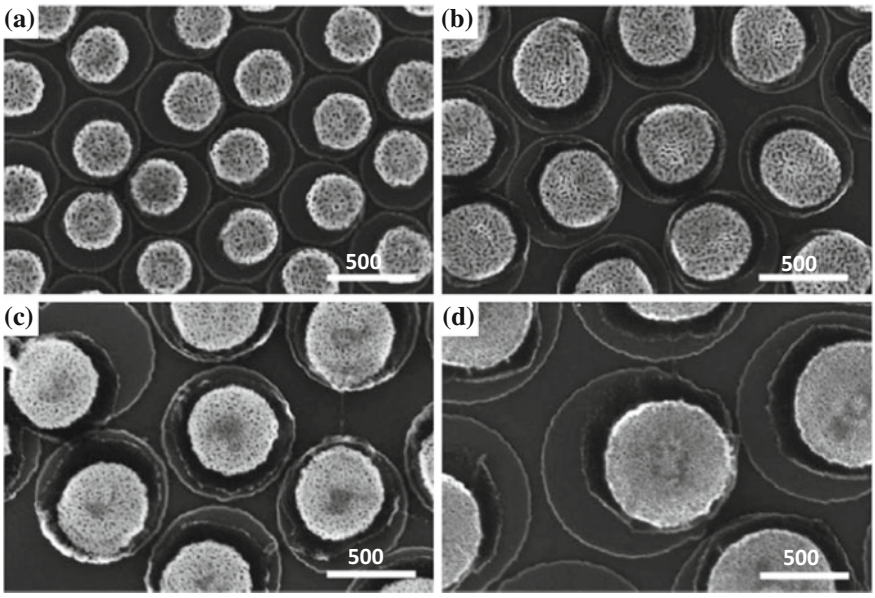

Fig. 3 SEM images of NPG disks made using 460 ± 9, 600 ± 12, 800 ± 9 and 1100 ± 14 nm PS beads on Si substrates. The corresponding final NPG disks diameters are **a** 300 ± 7, **b** 400 ± 10, **c** 500 ± 6 and **d** 700 ± 13 nm, respectively

acid (70% HNO_3 in water), followed by rinsing in deionized (DI) water (Fig. 2d) to produce an array of NPG disks. There was substantial size shrinkage during the PS bead etching step as well as the dealloying process. Scanning electron microscopy (SEM) images (Fig. 2e–h) show the corresponding nanostructures through the fabrication steps. To produce suspended colloidal NPG disks, high-density NPG disk arrays on a 3 inch Si wafer are further sonicated in DI water.

Figure 3 shows SEM images of monolayer samples of NPG disks on Si substrates made from PS beads with different diameters. The mean size and the standard deviation of different NPG disks are determined by measuring ≈100 disks using SEM images for each set of samples. The small size dispersion confirms the high fidelity of the pattern-transfer process.

Compared to the original sizes of the PS beads, there is an approximately 33–37% decrease in the NPG disk diameter, of which ≈5% occurs during the oxygen plasma treatment and up to 32% occurs during the dealloying process. Similarly the thickness decreases by ≈30%. This is consistent with the volume shrinkage effect observed during the formation of nanoporous gold by electrochemical dealloying [20]. Simulations of geometric relaxation in bicontinuous nanoporous metals revealed that surface relaxation played a significant role in the dramatic shrinkage during selective dissolution [21]. We note that NPG disks have move off-center during the fabrication process and this can be attributed to the weakening of the adhesion between the Si substrate and the deposited Au/Ag alloy during HNO_3

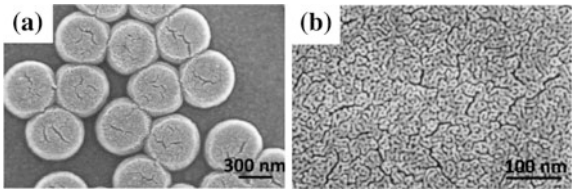

Fig. 4 **a** Top view of NPGDs ringed by gold; **b** unpatterned NPG film

dealloying through oxidation of Si to SiO_2. The strong stress generated by volume shrinkage leads to movements of the NPG disks. It is also worth noting that the weakened adhesion of the disks on the Si substrate is nevertheless sufficient to sustain rinsing with water. In contrast, NPG disks which are fabricated and strongly immobilized on a 300 nm Au film substrate as in [18] show cracks on their surface as can be appreciated on Fig. 4.

2.2 *Size and Porosity Characterization*

NPG disks prepared following the process described above can be easily released from the silicon substrate into DI water by sonication, due to their weak adhesion, to form colloidal NPG disks suspensions. Surfactant-free NPG disks are easily transferred into DI water without aggregation. The inset in Fig. 5c shows colloidal NPG disks dried on a Si wafer. Therefore, by flowing individual colloidal NPG disks in microfluidic channels, the single disk (400 nm diameter) buoyant mass is determined to be $6.04 \times 10^{-14} \pm 7.6 \times 10^{-15}$ g as shown in Fig. 5d. For comparison, 400 nm diameter Au disks without porous structures immediately form aggregates in the millimeter size range in an aqueous solution upon release from the substrate.

As an effort to understand the colloidal stability of the NPG disks suspensions in water, their zeta potentials are measured and presented in Table 1. In general, when

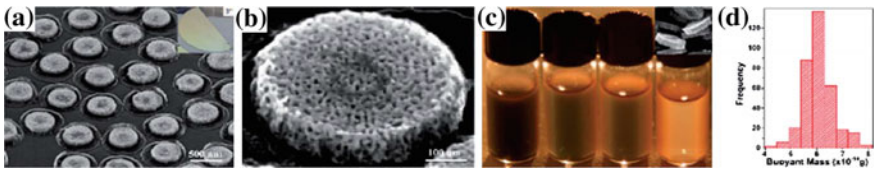

Fig. 5 SEM images of NPG disks taken at a 45° viewing angle, stored in DI water, and single disk buoyant mass measurements: **a** high-density NPG disk arrays on Si wafer before release. The inset is a 3 silicon wafer covered by a high-density monolayer of PS beads. **b** A single NPG disk with a diameter of 500 nm. **c** NPG disks having different sizes 300 ± 7, 400 ± 10, 500 ± 6, and 700 ± 13 nm (from left to right) after being released from the substrates by sonication in DI water to form colloidal NPG disk suspensions. The inset is the SEM image of NPG disks released from the substrate by sonication, dropped and dried on a Si wafer. **d** Histogram of 400 nm NPG disk buoyant mass distribution measured by flowing colloidal NPG disks in the microfluidic channel

Table 1 Average size, porosity and Zeta potentials for NPG disks 75 ± 1 nm thick. [a]NPG disks were made by using 460, 600, 800 and 1100 nm PS beads as masks and identical alloy thickness. [b]The roughness factor was obtained by using the expression $3h\beta/r$, where h, β, and r are the NPG disk thickness, two-dimensional porosity, and mean pore radius, respectively. [c]Zeta potentials were measured in DI water. [d]The full width at half maximum (FWHM) of the in-plane peaks of NPG disks obtained in air was measured by GRAMS/AI

NPG disk samples[a]	Average diameter (nm)	Average pore size (nm)	Roughness factor[b]	ζ(Mv)[c]	FWHM of the in-plane peak[d](nm)
1	300 ± 7	13.8 ± 2.2	6.56 ± 0.38	−28.5 ± 2.1	421.9
2	400 ± 10	13.7 ± 2.9	7.38 ± 0.41	−26.4 ± 3.2	460.9
3	500 ± 6	12.5 ± 2.0	7.71 ± 0.11	−19.0 ± 1.3	717.6
4	700 ± 13	12.8 ± 2.4	7.65 ± 0.27	−22.7 ± 1.2	1329.8

the absolute value of the zeta potential is larger than 25 mV, a nanoparticle suspension has a high degree of stability due to strong electrostatic repulsion between particles [22]. The zeta potentials of the 300 and 400 nm NPG disks suggests that both sizes of colloidal NPG disks have negatively charged surfaces and are quite stable in solution. Although the 500 and 700 nm diameter NPG disks possess negative surface charges but with slightly smaller zeta potentials, these larger NPG disks also exhibit practically useful long-term stability (i.e., no or minimal aggregation when stored in DI water at 4 °C for 4 months). The observed negative surface charge can be explained by the presence of deprotonated hydroxyl groups at the surface of NPG disks in aqueous solutions, which could plausibly form during the dealloying process in nitric acid. Another contributor to the NPG disks colloidal solutions stability could be the reduced inter-particles van der Waals forces due to their surface roughness which limits contact between particles.

The roughness factor of the NPG disks is estimated from the SEM images of the surface following a procedure described in [23].

2.3 *In-Plane Dealloying*

The fabrication of nanoporous gold disks described above involved pre-patterning alloy thin films into individual alloy disks *before* dealloying and thus can be classified as pre-dealloying modifications. Although highly effective, the dealloying rate using concentrated nitric can be as high as hundreds of nanometers per second, thus making the precise control and observation of the dealloying progresses challenging. In the method described in Sect. 2.1, unrestricted dealloying typically occurred from all fronts where Ag atoms were met with nitric acid and then dealloying propagated three dimensionally throughout the alloy, producing the internal nanoporous network.

In [24], a novel in situ NPG patterning method is introduced which generates hierarchical NPG structures during the dealloying process. In situ patterning is

achieved by limiting the initiation point of dealloying to designated locations and restrict the reaction to only progress in-plane. After forming a film stack of an optional adhesion layer, an alloy film, and a Cr layer, the PMMA (poly(methyl methacrylate)) photoresist is deposited by spin-coating onto the surface, exposed by SEM equipped with a nanopattern generation system and developed, leaving a PMMA mask containing the via patterns on the top Cr layer. Next, the pattern is transferred from PMMA to the Cr layer by wet etching. A timed-immersion in concentrated nitric acid for dealloying follows. Due to the protection provided by the Cr layer, nitric acid could only etch the alloy through the openings, and then progressed in-plane or laterally. By controlling the dealloying time, NPG disks with various diameters are fabricated during dealloying. Experiments show that the dealloying distance is linearly proportional to dealloying time.

The smallest NPG disk that can be fabricated with in-plane dealloying is limited by the smallest via diameter and the precise dealloying time control. Since 20 nm via diameter can be routinely achieved by commercial e-beam writers, together with the wet etching undercut, 30 nm diameter via is achievable. Combining with the slowest dealloying rate 43 nm/s measured in the experiment with the conditions estimated above, the minimum diameter is 460 nm. Since the size of the NPG structure and the size of the pores are both controlled by the dealloying time, with this method, the size of the pores induced by dealloying cannot be tuned independently.

2.4 In Situ Laser-Assisted Dealloying

In [25], another in situ NPG micropatterning method is presented; the patterning is realized by localized laser heating, during which dealloying occurs at the laser focal spots due to elevated temperature. It has been shown that the dealloying rate increases with rising temperature and decreases with lowering acid concentration [26]. Therefore, dealloying can occur at elevated temperature even in diluted acid which otherwise has negligible dealloying effects at room temperature. Laser-induced localized heating can be utilized through the concomitant use of a spatial light modulator and design and fabricate NPG micropatterns on substrates immersed in an aqueous environment with diluted nitric acid which otherwise has negligible dealloying effect.

2.5 Integration of the NPG Disks into a Microfluidic Device

Microfluidic platforms hold great promise in achieving detection and identification of biomolecules in low cost as well as point-of-care applications due to their distinct advantages such as small sample and reagent consumption, fast reaction and analysis times and low cost. Among the variety of methods which have been

implemented within microfluidic systems for molecular sensing, Surface-Enhanced Raman Scattering (SERS) based detection techniques have a prominent role due to their molecular specificity, label-free and multiplexed sensing capabilities. SERS harnesses the strong local electromagnetic field intensity enhancement at the surface of metal nanoparticles at plasmonic resonances to increase by several orders of magnitude the Raman scattering from a molecule near the metallic surface [9].

There are two main approaches in designing a SERS-based microfluidics detection system. One is based on colloidal metal nanoparticles acting as Raman enhancers dispersed in solution, which interact with analytes of interest and adsorb them onto the surface via mixing before SERS measurements are conducted [27, 28]. In general, SERS intensities depend on the degree of colloid aggregation that is significantly influenced by sample properties such as ionic strength and controlled by addition of aggregating agents such as potassium chloride. Clusters of different sizes and trapping different amounts of the analytes are produced and complicate the interpretation of the statistics of SERS intensities.

Another approach is that of integrating nanostructured metal surfaces as SERS-active substrates directly into the microfluidic platform. The existing nanostructure-integrated microfluidic SERS sensors primarily use silver. Although Ag-based SERS substrates provide inherently higher SERS enhancement compared to Au-based ones, the long-term stability is worse due to the gradual degradation of Ag surfaces [29]. Although the nanostructured surface approach typically provides better robustness against sample conditions, the amount of molecules that can effectively interact with the nanostructures is quite limited by diffusion—as low as <1% can be estimated using a simple boundary layer analysis in a largely laminar flow situation [30].

To address the diffusion limit mentioned above, a strategy is to increase the total usable area of the nanostructured surface, which provides more adsorption sites for biomolecules. As presented earlier, the NPG disks have large specific areas and high roughness factor (see Table 1) and we will see later that they possess a high density of plasmonic hot spots, high photothermal conversion efficiency and high SERS enhancement factor [18, 31, 32]. In the following, the design and fabrication of nanoporous gold disks monolithically integrated inside a microfluidic chip is described [33].

Figure 6 schematically illustrates the fabrication process for the NPG disk sensor, which is accomplished by oxygen-plasma bonding of two constructs: a SERS-active glass coverslip substrate with patterned NPG disks arrays and a poly-dimethylsiloxane (PDMS) layer containing a microfluidic network. The overall fabrication process includes a single low-cost transparency mask and four major steps: (a) definition of the SERS detection area, (b) construction of the NPGD arrays, (c) patterning of the microfluidic channel, and (d) plasma bonding.

The first step (a) produces a confined SERS detection area within the microchannel network, in which a photoresist mold containing microchannel structures are built using standard photolithography techniques through a transparent mask having the structures of the desired microchannel network (see Fig. 6(I)).

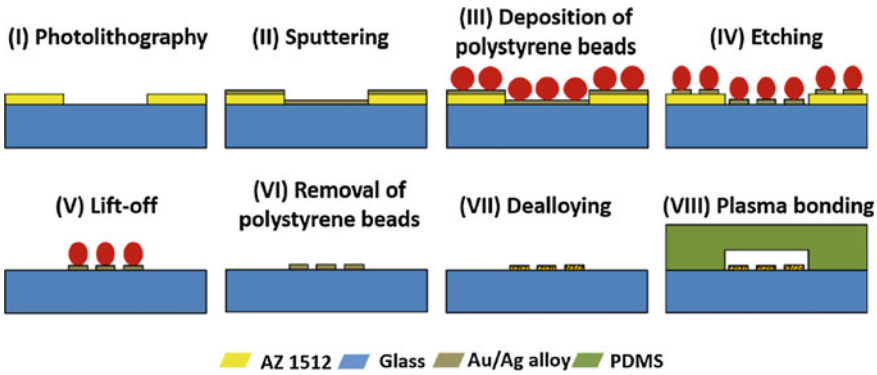

Fig. 6 Schematic view of the fabrication process for the surface-enhanced Raman scattering SERS-active nanoporous gold disk arrays within a microfluidic channel. (I) AZ 1512 in yellow is the UV sensitive photoresist. (II) In [33], the chosen alloy atomic ratio is $Ag_{82.5}Au_{17.5}$. (III) The self-assembled monolayer consist of closely packed 600 nm PS beads

Then, (b), SERS-active NPGD arrays are fabricated within the predefined region for SERS detection by generic polystyrene beads nanosphere lithography as described earlier in the chapter. Once the closely packed PS beads monolayer has been deposited (see Fig. 6III), the glass coverslip is treated with two steps of plasma etching in Fig. 6IV: oxygen etching to shrink the PS beads and argon sputter etching to etch away the portions of alloy film unmasked by the PS beads. A lift-off process is then conducted to remove the photoresist and all the nanostructures on its surface (Fig. 6V), leaving only alloy disks and PS residues within the predefined SERS detection region designed during step (a). After removing the PS residues (Fig. 6VI) by sonication in chloroform for 1 min, and dealloying of silver (Fig. 6VII) in concentrated nitric acid for 1 min, NPGD arrays with the designed geometry are formed on the coverslip. Due to the internal nanoporous network, the fabricated NPGDs have a large specific surface area for molecular adsorption sites.

The next step (c) is the patterning of the matching microfluidic channel. The PDMS microfluidic channel is fabricated using a soft lithography technique [34]. SU-8 negative photoresist is patterned through a standard photolithography technique to create a positive relief of the microchannel pattern on the surface of a silicon wafer. The pattern of the microfluidic network is designed to match the SERS detection region on the coverslip. Thus, the same transparent mask used previously in step (a) is employed here. Then liquid PDMS prepared by mixing a base and curing agent at a weight ratio of 10 : 1 is poured over the master, degassed, and cured in a vacuum oven. The negative PDMS cast with the microchannel pattern is then peeled off the master, and two via holes are punched for fluidic access.

The final step (d) consists in closing the microfluidic device to form enclosed channels covered by NPG disks arrays. Both the top surface of the prepared

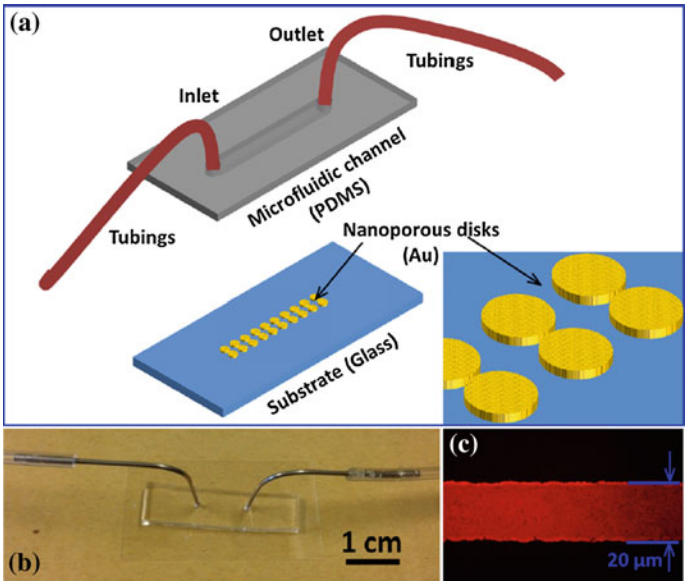

Fig. 7 microfluidic sensor architecture. **a** Preassembled parts consisting of the NPGD arrays coverslip and the PDMS microchannel network. The inset at the corner is an enlarged diagram showing the NPGDs; **b** photograph of the final sensor used in [33]; **c** a fluorescence microscopic image of the microchannel filled with Rhodamine 6G solution to confirm properly sealed microchannels

coverslip with NPGD arrays and the microchannel side of the PDMS layer are treated by oxygen plasma. After that, both surfaces are covered with methanol acting as a lubricant, and are precisely aligned under a microscope for face-to-face contact then heated at 90 °C for 5 min. Figure 7 shows a schematic of the assembled device together with a visual image of the final sensor utilized in the experiments in [33].

3 Optical Properties of NPG Disks

Semi-infinite dealloyed nanoporous gold (NPG) films with their unique bicontinuous structure of nanoscale ligaments and pore channels possess interesting optical properties, originating from the surface plasmon resonances (SPR), such as mixed states of localized/propagating surface plasmons [35, 36]. The intensity and peak position—i.e., wavelength at which absorption and scattering of light through excitation of the SPR are maximum—strongly depend on the nanopores size and the characteristic lengths and sizes of the ligaments [37]. In "as-dealloyed" NPG thin films, the LSPR band centering around 600 nm has a limited tunability of about 50 nm, achieved by varying the pore size from 10 to 50 nm [16]. In

mechanically stamped NPG thin films, the grating modulation provides a propagating SPR mode coupled with NPG's original LSPR band [38]. However, the plasmonic landscape is dominated by the NPG LSPR. Furthermore, in thermally wrinkled NPG thin films, random, sparse plasmonic hot-spots form at gaps and junctions due to structural deformation, and thus do not alter the average plasmonic behavior [17].

NPG disks however, with their well-defined "exterior" disk shape of 300–700 nm with thickness around 100 nm, add a two-dimensional confinement to the "interior" three-dimensional porous network, which results in intriguing plasmonic properties.

3.1 Localized Surface Plasmon Resonances of NPG Disks and Their Size-Dependent Tunability

3.1.1 Extinction Spectra and LSPR Peaks

As shown in the extinction spectra in Fig. 8a, three peaks have been assigned to NPG LSPR ("▲"), out-of-plane resonance ("■"), and in-plane resonance ("●"). The NPG LSPR mode originates from the nanoporous structures, whereas the in-plane and out-of-plane modes are associated with the external disk shape. Size-dependent plasmonic shifts in these peaks are observed when the disk diameter is increased from 300 to 700 nm. Among these peaks, the in-plane resonance clearly dominates and only exists in NPG disks but not in semi-infinite NPG thin films.

The peak at 515 nm assigned to NPG LSPR ("▲") shows limited tunability with respect to pore size and ambient refractive index; a red shift of this peak to 540 nm in air was observed in [16] when the pore size was varied from 10 to 30 nm. In contrast, NPG disks have highly tunable plasmonic properties for all peaks as shown in Fig. 8a, due to plasmonic coupling between the nanoporous structures NPG LSPR and the patterned disk shape in-plane disk LSPR.

In addition, as seen in Fig. 8b, the out-of-plane resonance mode ("■") also exhibits a red shift with increasing disks diameter, whereas this mode resonance wavelength is fixed in the case of NPG films.

The plasmonic properties of NPG disks can be further understood by comparing with those of Au disks having the same diameter and thickness on glass substrates as presented in Fig. 8c. Compared to Au disks, the in-plane plasmonic band of NPG disks exhibit a remarkable red shift from 858 to 1100 nm which could be interpreted by plasmonic coupling [39] between the three-dimensional bicontinuous porous nanostructures and the outer geometrical size and shape. By normalizing the extinction spectra to their respective buoyant mass measured on a single-particle basis (Fig. 8d), it is evidenced that the peak height of the in-plane mode of NPG disks is about twice that of Au disks of the same external geometry. The NPG disk

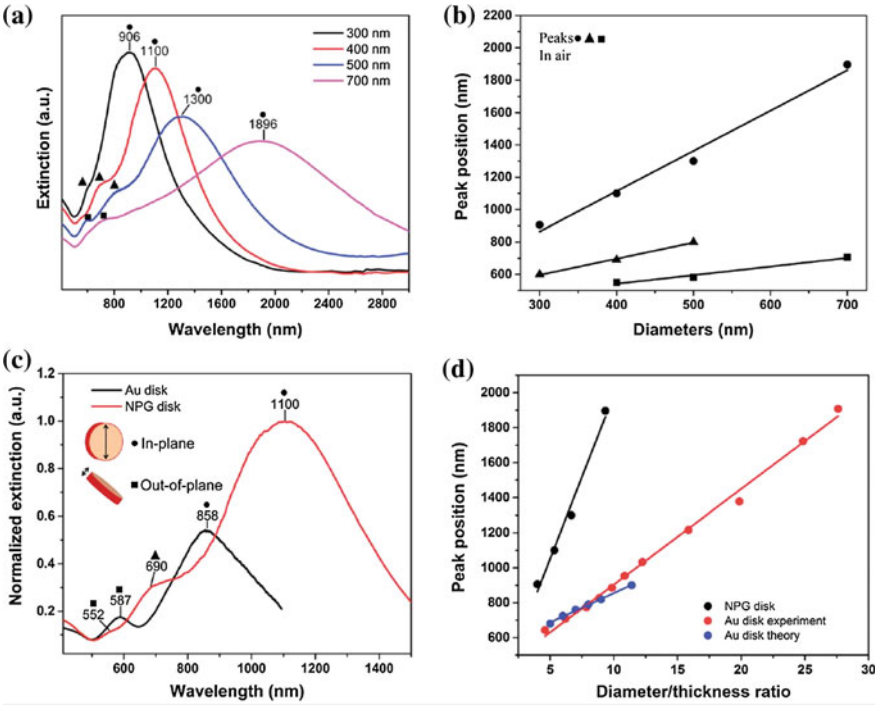

Fig. 8 Size-dependent plasmonic properties of NPG disk and comparison with Au disk: **a** extinction spectra of NPG disks with different diameters: 300, 400, 500, and 700 nm. The samples consisted of high-density NPG disk monolayers on glass substrates in air. **b** Plasmonic resonance peak positions versus NPG disk diameters in air. **c** Extinction spectra of 400 nm diameter and 75 nm thickness Au disks and NPG disks on glass substrates measured in air. Both spectra were normalized to buoyant mass. The inset shows the in-plane and out-of-plane resonance modes. **d** The in-plane dipole resonance peak positions are plotted as a function of the diameter/thickness ratio. The black circles represent NPG disks. The red and blue circles correspond to Au disks results from experiments in and theoretical calculations respectively. All extinction spectra were collected at normal incidence

also shows a much broader in-plane peak compared to the Au disk. Overall, the total extinction per buoyant mass for NPG disks is 3.3 times that of Au disks. The peak broadening can be attributed to random nanoporous structures and nanoscale Au ligaments.

Figure 8d shows the in-plane resonance peak position dependence on the diameter-to-thickness ratio (DTR). While Au disks in-plane resonance exhibits a 40 nm redshift per unit DTR increase, this redshift is 4.5 times larger for NPG disks suggestive of a much larger tunability by geometrical modifications.

The plasmonic tunability of monolithic NPG disks can also be explored by external and internal morphological changes. Specifically, increased dealloying time results in internal morphological evolution such as size growth of both the pore and ligament, thus further coarsening the porous network. Thermal annealing, in

contrast, introduces both external morphological changes such as disk thickness and diameter reduction, as well as internal modifications such as pore coalescence [40].

3.1.2 Electric Field Distribution and Localized Field Enhancement

The UV-visible extinction spectra presented previously give a measure of light absorption and scattering by the NPG disks per unit wavelength and indicate where the LSPR resonance frequencies are; these spectra are however recorded in the "far field" and the local distribution of the electromagnetic field over the metallic structures and its intensity are lost. The principle of enhanced optical spectroscopies such as SERS and SEF is to harvest the locally intense electromagnetic fields that are confined to "hot spots" which are the result of the excitation of the localized surface plasmons. Analytes that are in the immediate vicinity of these hot spots will experience a local EM field whose intensity and polarization can be dramatically different from the incident field and therefore will exhibit modified interaction with light (enhanced Raman scattering, enhanced, or quenched fluorescence).

Electromagnetic modeling and simulations can be used to elucidate the local response of the nanostructures to an incident electromagnetic field.

In Fig. 9, finite difference time domain (FDTD) simulations were performed for a NPG disk and compared with a bulk Au disk having identical external shape parameters: 500 nm in diameter and 75 nm in thicknesses. The NPG disk model shown in Fig. 9a was constructed directly from the SEM image in [41]. Figure 9c displays the calculated electric field distribution for the 1300 nm incident wavelength which matches the in-plane resonance previously discussed. The maximum field enhancement is $\approx$100 in the pores around the edge whereas the Au disk produced a maximum E-field enhancement of $\approx$15, confined to either side of the disk. At 785 nm excitation wavelength (matching the NPG LSPR peak), the hot sports are uniformly distributed within the entire disk and the maximum enhancement factor is about 32 versus 5 for the Au disk. Thus, the NPG disk maintains a sixfold higher E-field enhancement compared to the Au disk.

It is worth emphasizing that the hot spots distributions in the NPG disk for 785 nm and 1300 nm incident wavelengths display remarkable differences. At 1300 nm, the hot-spot distribution appears to be concentrated near the pores around edges, supporting our previous interpretation of coupling between the in-plane resonance and the pores around edges. In contrast, the uniform hot spot distribution for 785 nm supports the interpretation that it is solely from NPG LSPR excitation. Overall, the FDTD results provide further support that the plasmonic coupling originating from the random nanoporous structure and the disk shape plays a key role in the unique plasmonic properties of NPG disks.

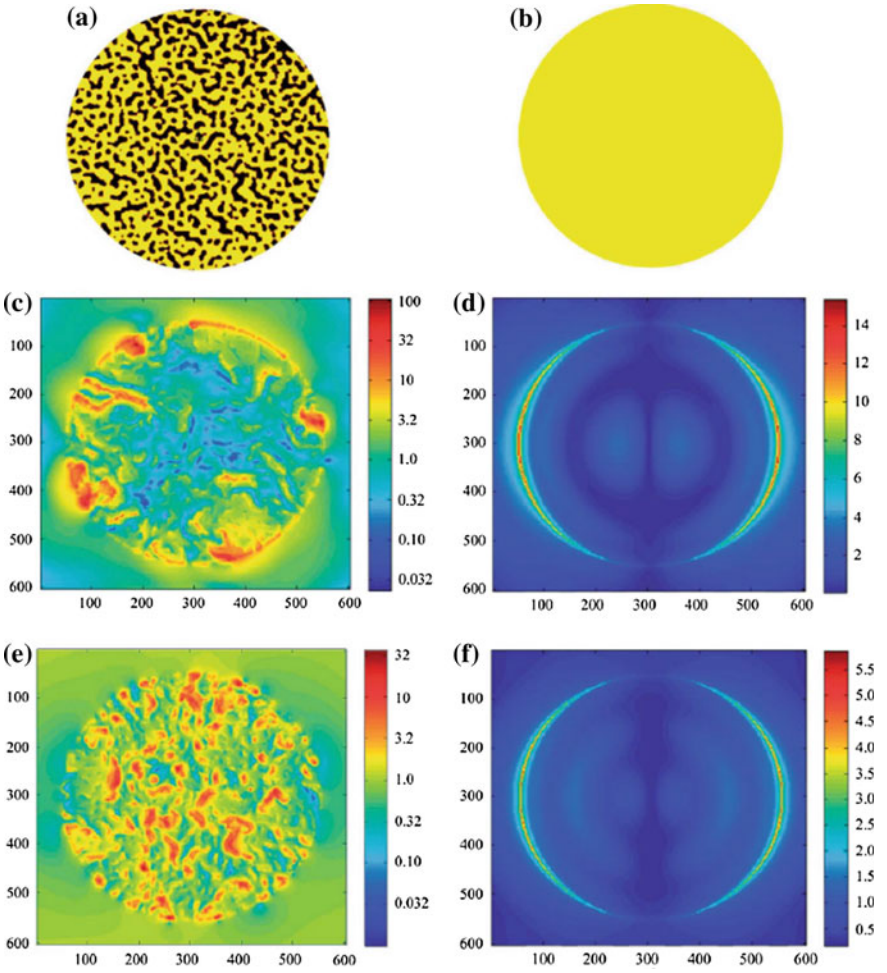

Fig. 9 E-field distribution of the NPG disk and Au disk with 500 nm diameter and 75 nm thickness: **a** and **b** are simulated models for NPG disk and Au disk, respectively. The E-field distribution was simulated using FDTD with plane wave incidence perpendicular to the disks, horizontally polarized. (**c** and **d**) E-field distribution of the NPG disk and Au disk for the 1300 nm incidence wavelength, respectively. (**e** and **f**) E-field distribution of the NPG disk and Au disk for the 785 nm incidence wavelength, respectively

3.1.3 Local Field Enhancement for SERS

Surface-Enhanced Raman Scattering (SERS) is a widely employed powerful spectroscopic technique which combines specificity—due to the uniqueness and sharp features of Raman spectra—and sensitivity, down to the single molecule, through the enhancement of the Raman signal by the excitations of plasmons at the surface of noble metal nanoparticles [9]. The enhancement of the signal is the

strongest when the analyte is in the immediate vicinity of the plasmonic hot spots on the metallic substrate. Hot spots are often associated with nanoscale gaps and protrusions [42] and are thus likely to be found in nanoporous gold with 5–20 nm pore diameters, nanoscale ligament sizes and/or thickness. An additional potential benefit is that internally adsorbed molecules and those that may be traversing the nanoporous network can also participate in Raman scattering. Several studies have been published on the use of NPG films as SERS substrates and wide variations in SERS enhancement factors (EF) have been reported [43, 44, 45] which reflects the differences in material composition and morphology due to the different fabrication techniques.

In this section, the SERS effect and related SERS EF on NPG disks is explored. Benzenethiol (BT)—also called thiophenol—molecules are chosen to be the Raman marker for they have the ability to form self-assembled monolayers (SAM) and thus enable the number of molecules on individual disks to be quantified. Furthermore, their absolute intrinsic Raman scattering cross section has been measured and utilized in SERS EF evaluation [46, 47]. The chosen excitation wavelength is 785 nm which is off electronic resonance for BT molecules and is particularly well-suited for biomedical applications due to the low absorption and fluorescence of cells and tissues in the near-infrared region of the spectrum [18]. Furthermore, inspection of Fig. 9 indicates that locally intense electromagnetic field can be produced on the surface on NPG disks by excitation of the LSPRs at 785 nm.

SERS enhancement factors are evaluated for BT SAMs deposited on unpatterned nanoporous gold films (NPG), NPG disks arrays and Klarite (commercial SERS substrate from Renishaw with an advertised SERS EF of 10^6) and the normal Raman spectrum of a neat solution of BT is recorded. Table 2 gives the estimated SERS enhancement factors at 785 nm for two fingerprint modes of Benzenethiol when compared to the enhancement measured on the Klarite substrate.

SERS spectra are normalized according to incident laser power, effective illumination area, and estimation of the number of BT molecules participating to the detectable SERS signal. The number of adsorbed BT molecules in and on an NPG disk is the product of the area of the disk, the roughness R of NPG (the ratio of the chemically active surface area to the geometrical surface area), and the BT surface density. The contribution of adsorbed molecules to the total SERS signal also decreases with depth because of the decreasing laser power density and increased absorption of the Raman scattered light and an effective roughness factor for SERS must be then calculated which takes into account the skin depth of gold and silver [48]. Such considerations show that the SERS effective surface area of a NPG disk is 6.3 times larger than its geometric area.

Table 2 SERS EF estimation using Klarite's enhancement as a reference

	Klarite	NPGD	NPG film
EF of 1076 cm^{-1}	1×10^6	1.05×10^8	2.03×10^5
EF of 1575 cm^{-1}	1×10^6	1.43×10^8	2.47×10^5

An alternative way to experimentally evaluate the SERS enhancement factor on NPG disks is to compare the SERS intensities of BT adsorbed in and on NPG disks with the Raman intensity of a neat BT sample measured in the same conditions [46]. Similar SERS EF for NPG disks are obtained by this method, i.e., an enhancement factor of about 5×10^8.

3.2 *Refractive Index Sensitivity of NPG Disks LSPR*

Plasmon resonances are sensitive to the refractive index of the medium surrounding the metallic nanostructures and exhibit peak shifts when there is a change in refractive index which are usually quantified by the sensitivity factor $d\lambda/dn$ with the units of nm per refractive index unit (nm per RIU). The sensitivity of LSPR peak positions to the immediate environment is the basis of LSPR spectroscopy.

NPG disks can be used as plasmonic sensors due to the excellent sensitivity factor [41]. To further extend the range of index sensing into those for common solvents, the peak shifts of 400 nm NPG disks were investigated over the index range of 1.36–1.495 using pure ethanol, ethanol–toluene mixtures, and pure toluene. Figure 10a illustrates the extinction spectra of the 400 nm NPG disks in these various solvents.

The in-plane and out-of-plane resonance peaks redshift with increasing refractive indices whereas the peak shift in the NPG LSPR peak is unclear due to the overlap with the broad in-plane resonance. Overall, the sensitivity of the NPG disk in-plane peak is larger than those of spherical Au nanoparticles, Ag@Au nanoshells, SiO2@Au nanoshells, Au disks, Au nanorods, nanocages and silver nanoprisms

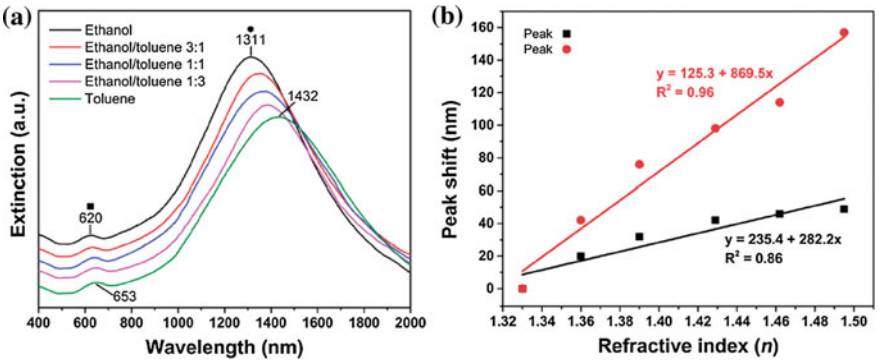

Fig. 10 **a** Extinction spectra of 400 nm NPG disks in various solvent mixtures with known refractive indices (n) varying from 1.36 to 1.495: ethanol (n = 1.36), 3: 1 ethanol–toluene (n = 1.39), 1: 1 ethanol—toluene (n = 1.429), 1: 3 ethanol–toluene (n = 1.462), and toluene (n = 1.495)0.16. **b** The peak shifts of in-plane peak (in red) and out-of-plane (in black) are plotted versus n

[49, 50, 51, 52] and comparable to nanorice [53] and nanorings [54] which range up to 800 nm per RIU.

4 Nanoporous Gold Disk Arrays in Microfluidic Sensing Applications

4.1 Microfluidic SERS Sensor with Monolithic NPG Disks Arrays for Rapid and Label-Free Dopamine and Urea Detection

The NPG disks are monolithically incorporated into the microfluidic device following the fabrication process described in Sect. 2.5. The schematic of the pre-assembled sensor is shown in Fig. 7. The height, width, and length of the microchannel are 20 μm, 20 μm and 1 cm respectively and the average diameter, thickness, and pore size of the disks decorating the microchannel are ~400, 75, and 14 nm, respectively [33]. SERS measurements are carried out on a Raman line-scan system at 785 nm [55]. The laser at the sample plane is shaped into a $1 \times 133\ \mu m^2$ line, yielding a spatial resolution of 1 μm and spectral resolution of about 8 cm^{-1}. The laser line is focused within the microchannel and scanned for hyperspectral area mapping.

4.1.1 Characterization of the Spatial Uniformity and Sensitivity of the Microfluidic SERS Sensor with no Flow

The dye rhodamine 6G (R6G) is used first as a model compound to test the robustness and uniformity of the sensor. A solution of R6G 1 mM in DI water is injected into the sensor via a syringe and let to rest for 10 min and SERS spectra are recorded from different areas onto the NPG disks surface of the microchannel. The relative intensity variations of major R6G peaks are calculated to be within 8% of the average intensity as shown in Fig. 11b, indicating the high uniformity and reproducibility of the NPGD sensor which is due to the highly uniform NPG disks arrays within the microchannel.

To further assess the sensing capability of the microfluidic sensor, concentration-dependent SERS measurements with R6G are performed, from 1 μM to 1 mM, with five recorded SERS spectra at different locations on the sample for each concentration of R6G, 10 min after injection. As shown on Fig. 12, the SERS peak intensities clearly increase with increased R6G concentrations. The intensity variations of the fingerprint mode 1366 cm^{-1} of R6G versus concentrations are used for quantitative evaluations. As shown in the inset, a highly correlated intensity-concentration relationship is obtained in the range 1 μM–1 mM. The limit of detection (LOD) is defined as the concentration at which the Raman intensity

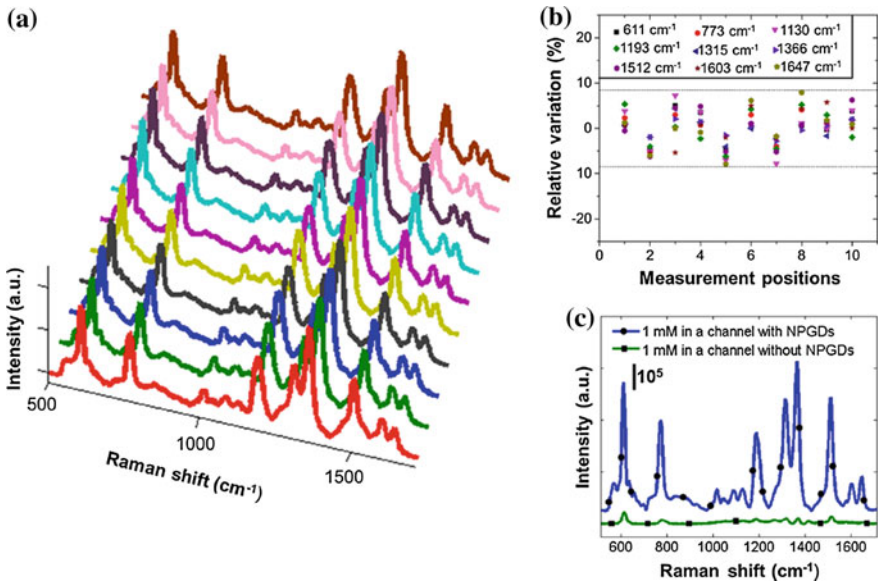

Fig. 11 R6G measurements **a** SERS spectra of 1 mM R6G detected in the SERS-active microfluidic channel at 10 different locations; **b** relative intensity variations of major peaks for the 10 locations; **c** spectra comparison of 1 mM R6G in a microchannel with NPGDs and a microchannel without NPGDs

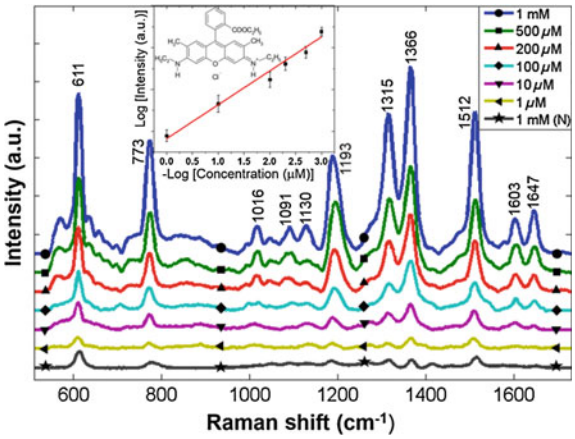

Fig. 12 Concentration-dependent SERS spectra of R6G measured in the sensor. The bottom trace was acquired from 1 mM R6G inside a microchannel without NPGD arrays. The inset indicates the variations of R6G peak intensity at 1366 cm^{-1} as a function of R6G concentration. The error bars represent the standard deviation from five measurements

value is equal to the averaged blank intensity at 1366 cm^{-1} plus three times the standard deviation.

4.1.2 SERS Detection of Rhodamine 6G with Continuous Flow

In addition to investigating the performance of the sensor without flow, its behavior under continuous flow is also studied. R6G solution at 100 μM is loaded into a syringe and injected into the sensor via a syringe pump at a flow rate of 3 μL/min. SERS measurements are recorded in situ under the continuous flow conditions with 2 s integration time per acquisition. Figure 13 shows the 1366 cm^{-1} mode SERS intensity variations within the first minute.

The starting point (t = 0 s) indicates the initial situation, where the NPGD arrays in the SERS detection region are not yet flooded by the sample solution. The signal intensity rapidly increases within the first 10 s, then steadily and slowly increases in the time range from 10 to 45 s, reaching a saturation limit in the last 10 s. After injecting the solution into the channel for 1 min, only small signal intensity variations (<10%) are observed, indicating the stability and robustness of SERS detection in continuous flow measurement. The dynamic behavior can be interpreted as follows: when more and more R6G molecules adsorb onto the surface of the NPG disks array, the SERS intensity keeps increasing within the first minute. The intensity reaches a quasi-plateau when maximum numbers of R6G molecules are adsorbed at a fixed flow rate. Further, the intensity achieved around 70% of that at the quasi-plateau state within the first 10 s. The result suggests that the sensor can provide rapid detection (i.e., <2 s) in solutions.

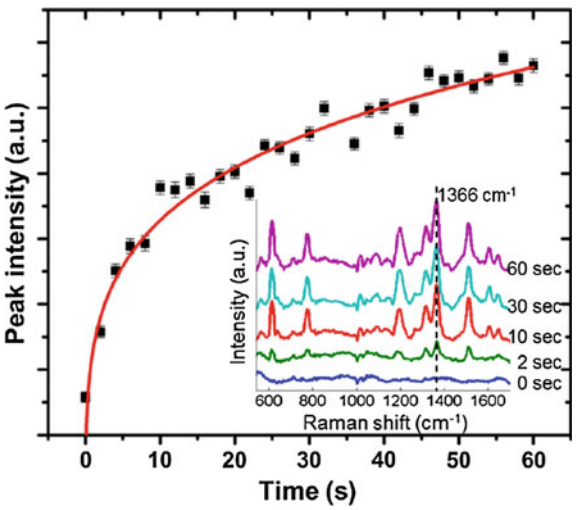

Fig. 13 Intensity variations versus time under the continuous flow condition. The 1366 cm^{-1} peak intensity of 100 μM R6G is plotted. The inset presents the measured SERS spectra at five selected time points of 0, 2, 10, 30, and 60 s

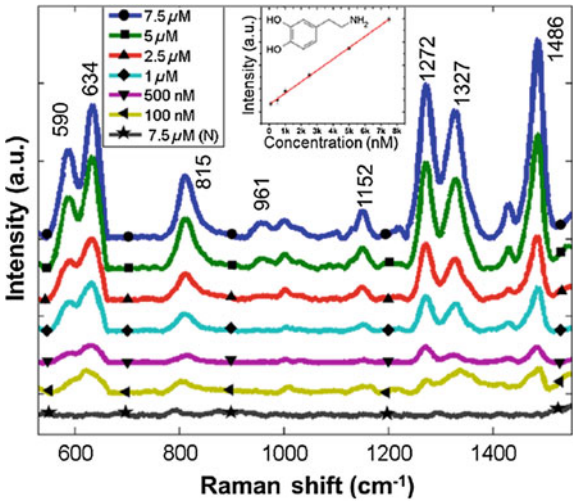

Fig. 14 Concentration-dependent SERS spectra of dopamine (DA) in the sensor. The bottom trace is acquired from 7.5 μM DA inside a microchannel without NPGD arrays. The inset shows the intensity variations at 1272 cm^{-1} with respect to DA concentration along with the molecular structure of DA. The error bars represent the standard deviation from five measurements

4.1.3 SERS Detection of Dopamine and Urea

Next, the capability of the sensor to detect dopamine, an essential neurotransmitter, is tested. Dopamine solutions of different concentrations ranging from 100 nM to 7.5 μM are introduced into the sensor by a syringe. After filling the microchannel for 10 min, SERS spectra are measured at five locations with 30 s acquisition time each. The averaged spectra are shown in Fig. 14 where the major Raman peaks of dopamine are clearly identified [56]. A good linear relationship is observed by plotting the SERS intensity at 1272 cm^{-1} versus concentrations as shown in the inset, and the limit of detection is calculated to be 32.4 nM.

4.1.4 SERS Detection of Urea at Physiological Concentrations

Artificial urine is prepared with 10 g of sodium chloride, 6 g of potassium chloride 6.4 g of sodium phosphate (monobasic, monohydrate) dissolved in 1 L of DI water and with concentrations in urea ranging from 1 to 20 mM. The corresponding SERS spectra are shown in Fig. 15, featuring the main Raman fingerprint of urea, the symmetrical C-N stretching mode around 1000 cm^{-1}. A good linear relationship is observed by plotting the SERS intensity at 1001 cm^{-1} versus concentrations as shown in the inset, and the LOD was calculated to be 0.67 mM with a power density of 0.21 $mW/\mu m^2$ and integration time of 10 s.

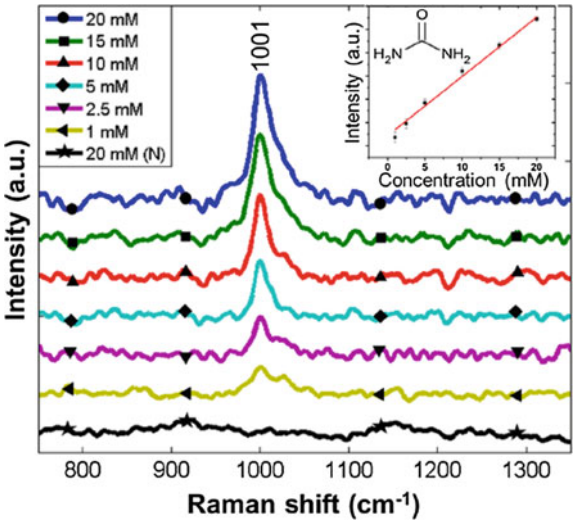

Fig. 15 Concentration-dependent SERS spectra of urea in the sensor. The bottom trace is acquired from 20 mM urea inside a microchannel without NPGD arrays. The inset shows the intensity variations at 1001 cm^{-1} with respect to urea concentration

The results suggest that the NPG disks based sensor provides a promising and versatile capability for clinical and diagnostic applications, such as kidney function monitoring and urine analysis.

4.2 In Situ SERS Monitoring of Individual DNA Hybridization in Microfluidics

DNA hybridization, where two single-stranded DNA (ssDNA) molecules form a duplex through non-covalent, sequence-specific interactions, is a fundamental process in biology and understanding its dynamics could help reveal molecular mechanisms involved in numerous biomolecular processes. To this end, sequence-specific detection of hybridization at the single-molecule level has become critical to many biomedical applications such as clinical diagnostics, biosensors, and drug development [57]. Current techniques to monitor diffusion and hybridization of DNA molecules include fluorescence correlation spectroscopy (FCS), single-molecule fluorescence resonance energy transfer (SMFRET), molecular beacons (MB), LSPR spectroscopy, electrochemistry and circular dichroism spectroscopy.

Label-free and amplification-free schemes are of particular interest because they could potentially provide in situ monitoring of individual hybridization events, and enable the discrimination of subtle variations due to single-base modification

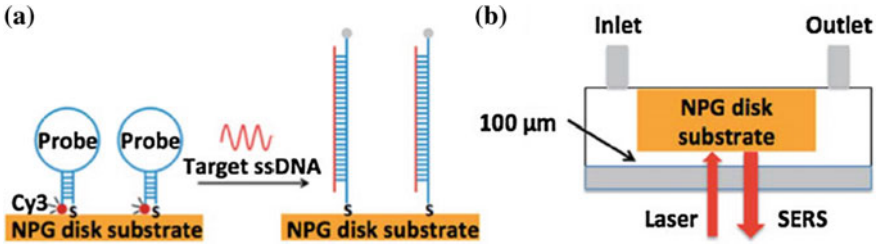

Fig. 16 Schematic of MS sensing mechanism in microfluidics

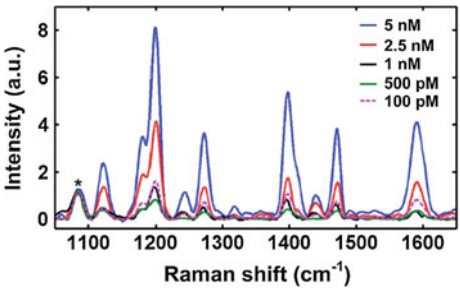

Fig. 17 SERS spectra of the MS probes on NPG disk substrates by incubation (500 pM–5 nM) and drop cast (100 pM) immobilization protocols

without stringency control or repetitive thermal cycling. SERS is an attractive approach for label-free multiplexed DNA/RNA detection because of its molecular specificity and potential single-molecule sensitivity and these distinct advantages have led to the development of a number of SERS sensing platforms for single DNA hybridization [58, 59].

In this section, the implementation of a microfluidic NPG disk-based sensor for in situ SERS monitoring of the same immobilized ssDNA molecules and their individual hybridization events is presented. To that end, molecular sentinels (MS, [60, 61]) are immobilized on NPG disks arrays inside a microfluidic channel, which prevents sample drying all the while keeping the sampled volume small. MS involves the design of the complementary sequence of a target ssDNA into a stem-loop "hairpin".

Figure 16 shows the schematic principle of MS use in a SERS experiment. The complementary hairpin probes have a thiol group at the 5′ end for robust immobilization on gold nanostructures and a fluorophore cyanine 3 (Cy 3) at the 3′end. Cy3 yields a strongly enhanced SERS signal when the probe is in the hairpin configuration; this signal decreases when the probe is hybridized with the target and moves away from the surface. The ssDNA target molecule is the ERBB2 gene, a critical biomarker of breast cancer and the hairpin probe consists of its complementary sequence (Fig. 17).

MS hairpin probes are immobilized onto NPG disk substrates at the bottom of a PDMS well by incubation for 40 min then the substrates are rinsed thoroughly in DI water and immersed in 6-mercapto-1-hexanol (MCH) for 10 min followed by

another DI water rinse. The substrates are then mounted inside a temperature-controlled microscope microfluidic cell culture stage and a syringe pump is used to deliver target solutions of known concentration for hybridization. SERS measurements are carried out with 785 nm excitation with a 133 μm × 1 μm line-shaped focus, as described previously in the chapter, yielding about 1 μm spatial resolution and about 8 cm^{-1} spectral resolution.

4.2.1 SERS Detection of Immobilized MS Probes

Figure 17 shows SERS line spectra from different concentrations of ERBB2-sentinel probes on NPG disk substrates by incubation (500 pM–5 nM) and drop cast (100 pM), respectively. The SERS spectra show the major Raman modes of Cy3 [62] which indicates that the probe molecules are in their hairpin configuration, with the 3'-Cy3 near the gold surface. In the following experiments, the Cy3 peak height at 1197 cm^{-1} is monitored as the SERS intensity indicator. The immobilized probe density of drop cast onto NPG disk substrates is estimated from the number of probe molecules pipetted onto the NPG disk surface for the 100 pM solution or calibrated against the SERS intensity obtained from concentration-dependent SERS measurements obtained from MS drop cast substrates ([63] Supplementary Information). The average MS probe density is found to be about 2 molecules/μm^2 for NPG disk substrates incubated in 1 nM probe solution.

4.2.2 In Situ Monitoring of DNA Hybridization with Varying Target ssDNA Concentrations

In the first series of experiments, 5 nM molecular sentinel solution is immobilized by incubation on the NPG disks along with target concentrations from 5 to 20 nM. The SERS monitoring begins when the substrate is mounted into the microfluidic chamber and spectra are recorded every 10–15 min.

Figure 18a shows the Cy3 intensities at 1197 cm^{-1} from the line spectra after introducing the target ssDNA molecules; the SERS intensity of the peak begins to decrease after introduction of the 20 nM target solution then reaches a plateau at about 170 min indicating the end point of hybridization, at 40% of the starting peak intensity. Measurements over another 40 min indicate that no further hybridization occurs, i.e., 40% of the immobilized probes do not react with the target ssDNA molecules. A plausible explanation for the incomplete consumption of all immobilized probes is inefficient mass transfer of target ssDNA molecules to the NPG disk surface. According to the adsorption kinetics model of biomolecules [30], only a tiny fraction of target ssDNA molecules are able to react with probes in the current diffusion-limited configuration.

Figure 18b shows the hybridization and plateau phase of experiments with different target concentrations and non-complementary ssDNA molecules together

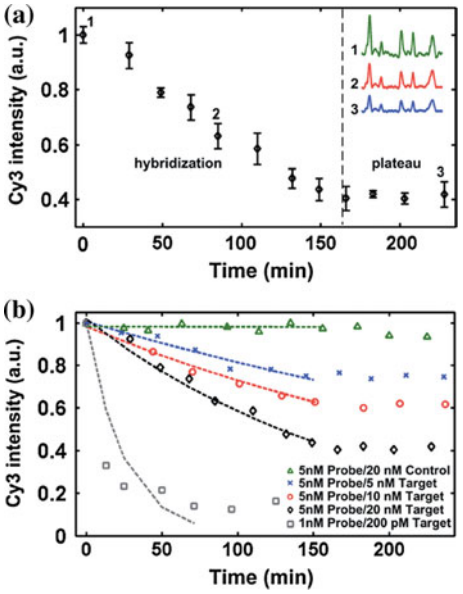

Fig. 18 In situ hybridization monitoring using SERS line spectra: **a** 5 nM MS probe hybridization with 20 nM target, **b** 5 nM MS probe hybridization with 5, 10, 20 nM target (cross, circle and diamond) and 20 nM non-complementary ssDNA (triangle); 1 nM MS probe hybridization with 200 pM target (square). Dashed curves are the exponential fits for the hybridization phase

with exponential fits of the data. The time constants increase with target concentrations, suggesting that target concentration can be determined by monitoring the decrease rate of Cy3 intensity. Alternatively, the final intensity value was also indicative of the target concentration. In the negative control experiment, 20 nM non-complementary ssDNA molecules do not cause a statistically meaningful SERS intensity change (≈5%). Furthermore, the stable SERS signal indicates that there is no photobleaching during experiments and the probe immobilization is robust. Thus, any signal decrease after adding target ssDNA molecules is attributed to hybridization.

To explore the detection limit in terms of number of target DNA molecules for the NPG disks sensor, the incubated concentration of MS probes is reduced to 1 nM for immobilization, resulting in a probe density of about two molecules/μm^2. After adding 200 pM target solution, the Cy3 SERS intensity decreases significantly in the first 10 min and reaches a plateau phase 90 min later. About 80% overall intensity decrease is observed.

Next, instead of the overall time trace extracted from the line spectra as shown in Fig. 18, individual time traces from point spectra are extracted by taking advantage of the spatial resolution of the line-scan Raman system. Ideally, there are 133 time traces using the point-spectrum, each scattered from a 1 μm^2 spot. Since the probe density is estimated to be about 2 molecules per μm^2 for substrates incubated in 1 nM MS probe solutions, and the average SERS intensities is 200 CCD counts, each 100 CCD counts is considered emanating from a single MS probe. Equivalently, each intensity decrease of 100 CCD counts during hybridization is attributed

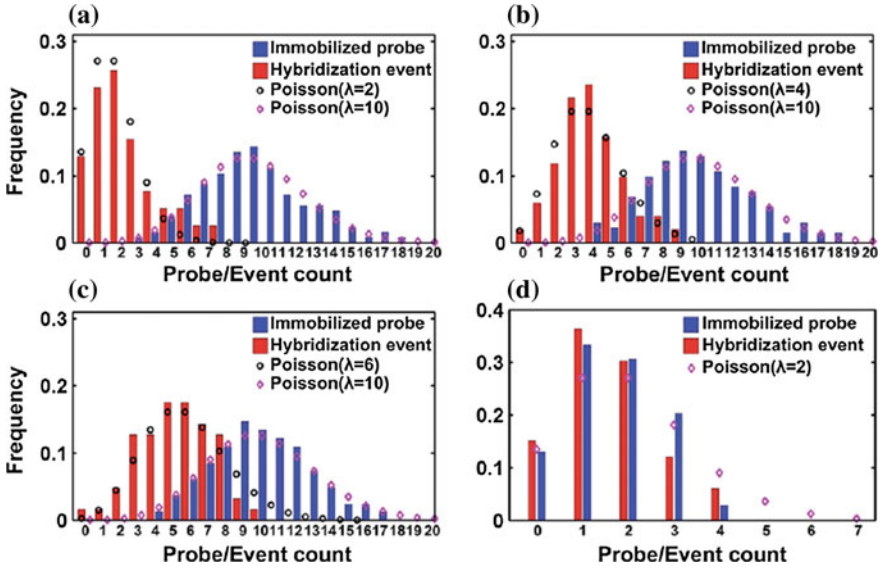

Fig. 19 Statistical analysis of individual time traces at probe/target concentrations of **a** 5 nM/5 nM, **b** 5 nM/10 nM, **c** 5 nM/20 nM and **d** 1 nM/200 pM. See text for details

to a single hybridization event. And an interval of 100 CCD counts between centers of bins is chosen in the following statistical analyses.

Figure 19 displays the histograms of immobilized probe count and hybridization event count by studying individual time traces. The point spectra showing high SERS intensities at different peak locations different from Cy3, likely from impurities in the solution, are excluded from the statistical study. The blue bars in Fig. 19 represent the frequency of the immobilized probe count on 1 μm^2 NPG disk surface before hybridization. These histograms (blue bars) can be better fit by a Poisson distribution than by a Gaussian with an average of 10 and 2 (shown as magenta diamonds) for substrates incubated in 5 nM and 1 nM probe solutions, respectively, in good agreement with the interpretation that 100 CCD counts represent a single probe. The red bars represent the frequency of hybridization event count. There are more hybridization events at higher target concentrations in 5 nM incubation experiments, which is consistent with the intensity time traces in Fig. 18b. Similarly, the histograms of hybridization event count can be better fit by a Poisson distribution (black circle in Fig. 19a–c, magenta diamond in Fig. 19d with averages of 2, 4, 6, and 2 for 5 nM, 10 nM, 20 nM and 200 pM target concentrations, respectively.

4.2.3 In Situ Monitoring of DNA Hybridization with 20 pM Target ssDNA Concentration

In these experiments, the probe molecules at 100 pM are immobilized by drop cast on the NPG disks resulting in about two probe molecules per μm^2 before hybridization. A protocol identical to the previous experiment is followed except that a 20 pM target solution is used.

Figure 20b–d shows the full-frame SERS images just before adding the target, during hybridization and at the last measurements (time points 1, 2, and 3 in Fig. 20a, respectively. As shown in Fig. 20f, the histogram (blue bars) of the immobilized probe count agrees well with a Poisson distribution with an average of 2 and a similar distribution is observed in the histogram of hybridization event count as discussed later. Four representative intensity patterns are observed and shown in Fig. 20e. The observation of quantized intensity decreases in individual time traces provide further support that individual hybridization events are observed.

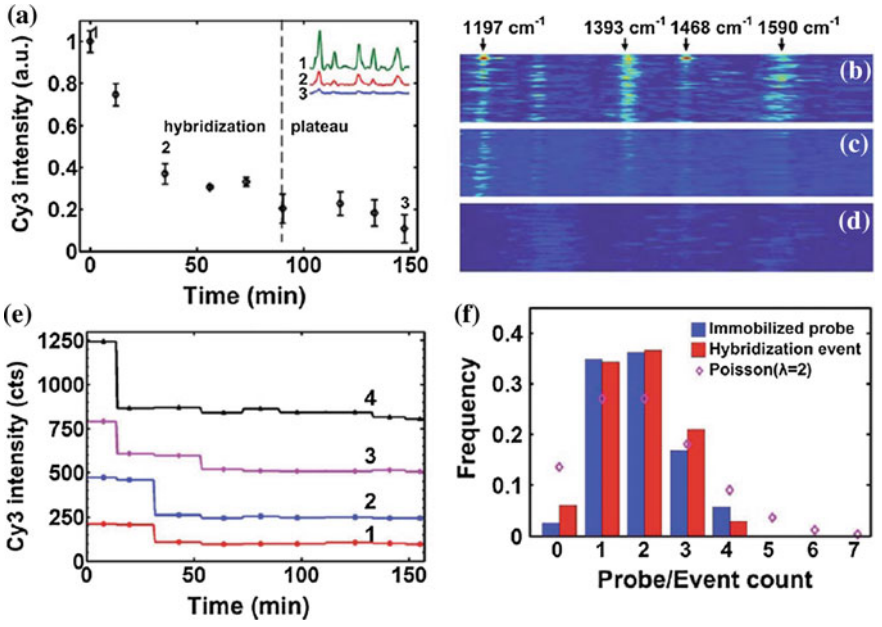

Fig. 20 **a** Overall Cy3 intensity trace with 20 pM target DNA; SERS image at **b** t = 0 min, **c** t = 40 min and **d** t = 150 min; the horizontal axis represents wavenumbers. Each row in the SERS image is a single point-spectrum. The major bands of Cy3 are labeled; **e** representative intensity patterns 1–4 corresponding to the hybridization counts 1–4 in **f** (red bars); (**f**) histogram analysis of individual time traces from 64 1 μm^2spots

5 Versatility and Performance: Nanoporous Gold Disk Arrays in Various Biomolecular Sensing Applications

5.1 Reagent and Separation-Free Measurements of Urine and Creatinine Concentration by Stamping SERS on NPG Disks Arrays

In this section, a novel method for the detection and concentration measurement of biological molecules by SERS is introduced. This technique, called stamping SERS (S-SERS) enables label-free, multiplexed molecular sensing and large-area and high-resolution molecular imaging. It also provides several benefits such as reagent and separation-free, low cost, high sensitivity and reproducibility [64, 65]. The performance of S-SERS is evaluated by the detection and quantification of creatinine spiked in three different liquids: creatinine in water, mixture of creatinine and urea in water, and creatinine in artificial urine within physiologically relevant concentration ranges. Finally, creatinine concentration measurements are realized for samples collected from a mouse model of nephritis, showing the potential for rapid, cost-effective, and reliable urine analysis for non-invasive diagnosis and monitoring of renal function.

Large-area, uniform, and reproducible NPGD arrays patterned on Au-coated silicon substrate are utilized as SERS substrates and SERS measurements are carried out with line-scan 785 nm laser excitation.

5.1.1 Stamping of the Analyte onto the SERS Substrate

First, a 1 μL droplet of the prepared solution containing the target molecules (i.e., creatinine) is first pipetted onto a PDMS thin film ($\sim$100 μm thick) laid flat on a glass coverslip. The droplet is then dried on the PDMS substrate, forming a film of target molecules after solvent evaporation. After that, a NPGD substrate ($\sim 0.5 \times 0.5$ cm^2) is gently stamped onto the PDMS surface bearing dried target molecules. Finally, the laser is focused at the PDMS surface to detect SERS signals arising from the sandwiched target molecules. Compared to directly drying the droplet onto the NPGD substrate, where target molecules are permanently chemically bound to the SERS substrate, the related issues like competitive adsorption among different molecules, surface and molecule affinity variability and uncertainty are reduced to some extent by the S-SERS technique.

The reproducibility of S-SERS creatinine is first tested; as shown in Fig. 21 the relative intensity variations of the major creatinine peaks are calculated to be within 12% of the average intensity, when repeatedly assayed from different locations on the sandwiched area.

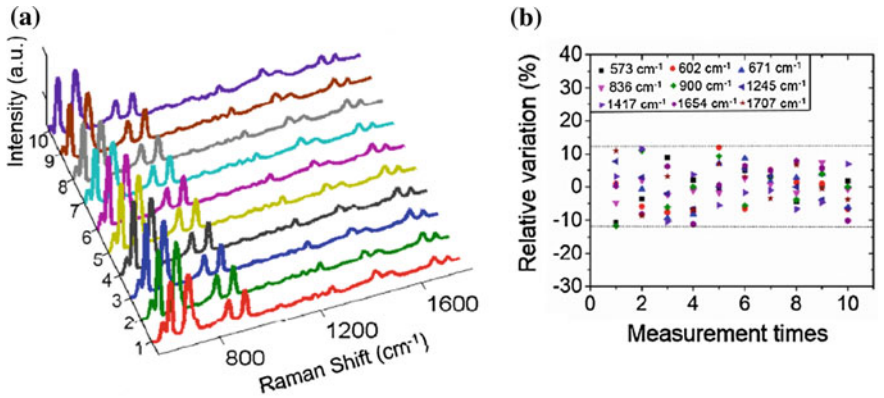

Fig. 21 Reproducibility of S-SERS: **a** SERS spectra of 100 μM creatinine detected by S-SERS at ten different locations, and **b** relative intensity variations of major peaks for the ten locations

5.1.2 SERS Detection of Creatinine in Water and Multiplexed SERS Concentration Measurements

Creatinine concentration-dependent SERS spectra are recorded for concentrations ranging from 100 nM to 100 μM in DI water. As expected, the SERS intensity of the major creatinine Raman peaks increases with increasing concentrations and the relationship is linear between the intensity variations of the 836 cm^{-1} peak and creatinine concentration within the whole [100 nM–100 μM] range. The limit of detection of creatinine in water is then estimated to be 13.2 nM based on the signal-to-noise ratio at 100 nM [65].

Next, the multiplexed sensing capabilities of urea and creatinine of the S-SERS sensor are tested. Since urea is a dominant chemical constituent in urine samples, a reagent- and separation-free technique needs to provide selectivity based on intrinsic molecular fingerprints. As presented in Fig. 22, measurements are performed on samples by mixing 100 μM creatinine and 100 mM urea solutions at five different volume ratios. Both concentrations ranges correspond to physiological concentrations in urine and are hence relevant for practical urine analysis. The results show that concentration-dependent creatinine SERS can be obtained even in the co-presence of $\sim 100 \times$ higher concentration of urea.

5.1.3 SERS Detection of Creatinine in Nephritic Mouse Urine Samples

Urine samples are collected from nephritic mice with anti-GBM disease [66]. The creatinine concentrations in these samples from different mice were first determined using a commercial colorimetric assay kit based on a coupled enzyme reactions with a specified detection limit of about 0.15 mg/dl. The entire assay from warming

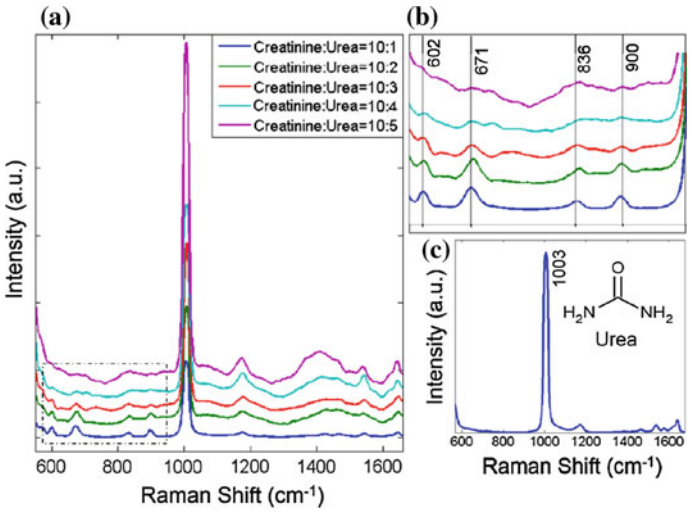

Fig. 22 SERS spectra from creatinine and urea water mixture **a** concentration-dependent SERS spectra of 100 μM creatinine and 100 mM urea mixed at different volume ratios. **b** zoomed-in view of the dashed window in (**a**), showing the intensity variation of creatinine. **c** Raman spectrum of urea in water

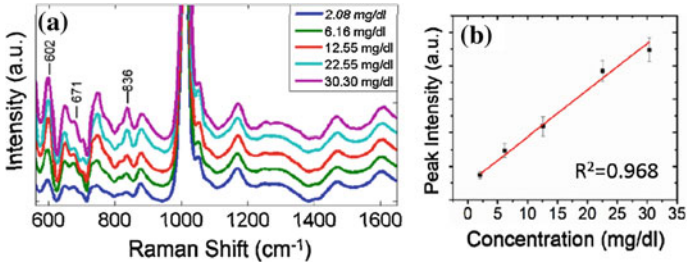

Fig. 23 Performance of S-SERS on urine from diseased mouse models: **a** Concentration-dependent SERS spectra of creatinine in urine samples collected from a nephritic mouse model of anti-GBM disease. **b** Variations of creatinine peak intensity at 836 cm^{-1} versus creatinine concentration

up reagents to room temperature to calculating creatinine concentration takes 1 h at the very least.

Figure 23a shows averaged SERS spectra of the different mouse urine samples with the concentrations determined by the assay test. A good linear relationship is observed by plotting the peak intensity at 836 cm^{-1} versus creatinine concentrations. When one compares the creatinine peak intensity at $\sim$836 cm^{-1} from real urine to that of creatinine water solution at the same concentration, one finds that the intensity from real urine is about six-fold lower than that from the creatinine water solution which may come from local refractive index differences between

water and urine, causing light attenuation and scattering. It is remarkable that S-SERS is still able to capture the creatinine-specific signature despite the co-existence of >70 different proteins in these nephritic urine samples [66].

5.2 NPG Disks Functionalized with G-Quadruplex Moieties for Sensing Small Molecules

In this section, a device for label-free SERS detection of malachite green (MG) is designed. NPG disks are functionalized with stabilized Guanine-quadruplex (G4) moieties with a highly specific topologic structure and effectively and selectively capture MG molecules for high sensitivity SERS measurements [67].

G4 are readily formed by the $\pi - \pi$ stacking of two or more G-tetrads prevalent in guanine rich (G-rich) oligonucleotides. These tetrads consist of a planar arrangement of four guanine bases held together by a cyclic array of Hoogsteen hydrogen bonds. The central core of the G4 is negatively charged due to the orientation of the carbonyl group of each G-base toward the center of the G-tetrad [68]. This configuration is believed to favor the conjugation of cations and small cationic organic molecules to the G4 structure [69, 70] and to enable ligand-specific binding into the G4 scaffold by varying its loop size and conformation [71] and the interaction between MG molecules and specific G4 scaffolds has been studied [72].

Malachite green (MG) is a well-known triphenylmethane dye with good antibacterial, antifungal, and antiparasitic properties. MG is commonly employed as an active ingredient in veterinary drugs to resist fungal and parasitic infections in aquaculture due to its low cost and availability but its use has however been restricted or prohibited due its potential carcinogenicity [73]. As a result, the European Union has mandated a sensor detection limit of 2 parts per billion (ppb) ($\sim$5.48 nM) for total MG and its reduced leuco-form. In addition, the U.S. Food and Drug Administration (FDA) prohibits the use of MG in aquaculture, hence a robust and reliable analytical technique is needed for effective detection of MG in aquaculture products, especially the fish meat sold for consumption.

5.2.1 Design of the Label-Free SERS Sensing Platform

NPG disks with 360 nm diameter are fabricated and form a semi-random array on the surface of a silicon wafer. SEM micrographs reveal the final nanoporous network with pore sizes of $\sim$15 nm in each individual disk [67]. NPG disks are then functionalized with G4 moieties stabilized by K^+ ions and 6-mercaptohexanol (MCH) is applied to block the nonspecific binding of small molecules. Exposure of the G4-decorated NPG disks to MG molecules causes the electron-rich phenyl rings of MG to effectively bind on the face of the G4 moieties to form G4-MG

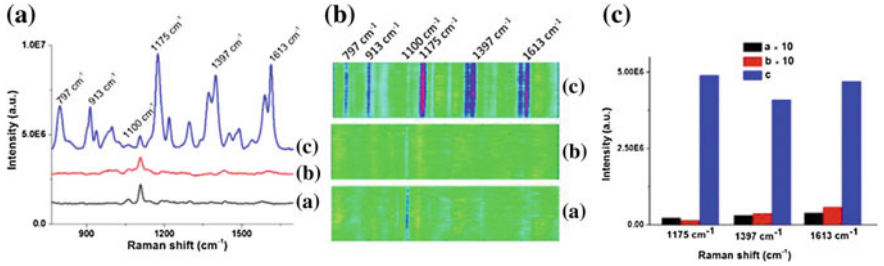

Fig. 24 **a** SERS spectra at 785 nm excitation and power 22.1 mW and **b** CCD image of different modified NPG disks; (**a**) MCH functionalized NPG disks immersed in MG solution (i.e., no G4); (**b**) G4-functionalized NPG disks immersed in buffer solution (i.e., no MG); **c** G4-functionalized NPG disks immersed in MG solution. (**c**) The corresponding SERS intensity from panel B at 1175 cm^{-1}, 1397 cm^{-1}, and 1613 cm^{-1}. The intensities from panels a and b were multiplied by 10 to be visible. The G4 concentration and MG concentration were 1.0 μM and 50 μM, respectively

conjugations through $\pi - \pi$ stacking and electrostatic interaction between MG and the G4 scaffold further improve the stability of the G4-MG complexes.

As can be seen in Fig. 24, remarkable SERS signal can be observed from the captured MG molecules on the G4-functionalized NPG disks. In contrast, no SERS signal, except for that from MCH molecules at 1100 cm^{-1}, is detected in the absence of MG molecules due to the lack of MG molecules being captured by G4 moieties. Similar results are obtained in the absence of G4 moieties, which suggests that MG molecules cannot be immobilized effectively onto the surface of MCH-incubated NPG disks without G4 as the capturing scaffold as well as the effectiveness of MCH as a blocking-agent. In contrast, the MG SERS intensity shows no significant variation in the presence of G4 before and after incubating with the MCH solution (Supplementary Information in [67]), which indicates that the MCH molecules cannot replace MG molecules that are captured by G4 moieties. In other words, the MG molecules are conjugated onto the surface of NPG disks through an interaction with G4 moieties rather than nonspecific binding on the surface of NPG disks, a key factor for high specificity.

It is found through G4 concentration studies of the evolution of the SERS sensitivity that the SERS intensity is enhanced sharply with increasing G4 concentration in the range of 100 pM–100 nM due to an increase of capturing sites formed on the NPG disks. However, the intensity increase slows down and reaches a plateau in the range from 100 nM to 1 μM. To achieve best performance, 1 μM G4 concentration is used in the following section.

5.2.2 Sensitivity for MG Detection

SERS measurements are obtained for a series of MG concentrations and presented in Fig. 25 The SERS intensity increases with the MG concentration from 50 pM to 5 μM, at which it reaches a plateau indicative of a reduction in binding events of

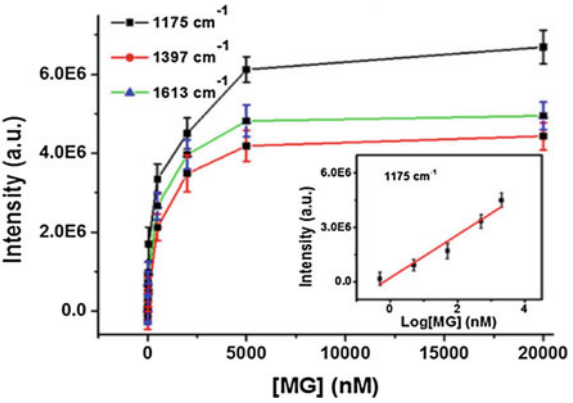

Fig. 25 SERS intensity for three fingerprint peaks of MG as a function of MG concentration. Inset shows a linear relationship between the SERS intensity at 1175 cm^{-1} and the logarithm of MG concentration at the range from 0.5 nM−2 μM. The error bars are calculated from at least three measurements on random spots on the same substrate

MG molecules onto the surface of G4-functionalized NPG disks. The prominent peak at 1175 cm^{-1} can be observed at 50 pM of MG which is 100 times more sensitive than the sensor detection limit mandated by the European Union for MG detection. The high sensitivity may be attributed to three factors: (1) the high enhancement of local electromagnetic fields from high-density hot-spots on NPG disks; (2) the high affinity of G4 moieties formed by the unique G-rich DNA to MG molecules; or (3) the nanoporous structure of NPG disks provides a high surface-to-volume ratio for loading more G4 moieties, thus capturing more MG molecules onto the surface of NPG disks (Fig. 25).

5.2.3 Sensor Performance in Complex Samples and Real-World Situations

The performance of the NPG disks sensor is evaluated on samples consisting of fish meat spiked with different MG concentrations as a model. Fish is purchased and turned into a homogenate, 2 g of which are then mixed with 10 mL PBS buffer solution and incubated at room temperature overnight. The solution is then filtered through a 0.22 μm membrane filter and various MG concentrations are used to spike the resulting supernatant.

As shown in Fig. 26, sensor performance similar to the above section is obtained for the complex mixture. Therefore, the proposed sensing system may be extended to other target assays in the biological and environmental fields while taking into account the possible need to modify the G4 sequence to accommodate for the target analyte.

Although the above-mentioned SERS sensor exhibits excellent sensitivity and good specificity, a laboratory Raman system has been employed for the SERS measurements. To demonstrate real time, onsite measurement in the field, the feasibility of the SERS detection with a portable Raman system with an optical fiber probe is tested, first on MG solutions in PBS and then on fish homogenates spiked with MG.

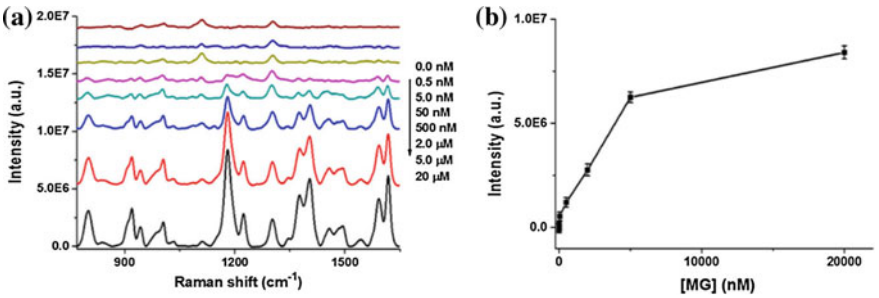

Fig. 26 **a** SERS spectra in fish samples spiked with various MG concentrations; **b** the corresponding SERS intensity change at 1175 cm^{-1}

Figure 27 summarizes the results and shows that the filter probe gives results similar to the laboratory Raman system. The lowest detectable concentration of MG with this system is 5.0 nM, which suggests that this NPG sensor can be effectively employed with a portable Raman system for onsite measurements for industrial and environmental applications. The difference between the linear relationships reported in Fig. 26 and that in Fig. 27 is due to the lower sensitivity of the portable Raman system compared to the line-scan system.

5.3 *Label-Free, Zeptomole Cancer Biomarker Detection by Surface-Enhanced Fluorescence on NPG Disks Arrays*

In this section, a label-free, spacer-free biosensor that makes use of distant-dependent detection of surface-enhanced fluorescence (SEF) is constructed on NPGD arrays and tested for ultrasensitive detection of ERBB2 cancer gene DNA targets [74].

SEF—also called metal-enhanced fluorescence (MEF)—occurs when fluorophores are within nanoscale proximity from surfaces of metallic nanostructures. Through the use of specifically designed metal nanostructures, increased fluorescence enhancement factors up to 500 times has been reported [75] and enhancements in the order of 5–50 times are typically observed [76, 77, 78]. When fluorophores are near metal surfaces, electronic energy transfer from the molecule may occur which generally leads to fluorescence quenching. Therefore, the fluorescence measured on "naked" metallic substrates is typically the outcome of the competition between SEF and metal-induced quenching and it is now understood that quenching occurs for nanoparticle-fluorophore distances smaller than 5 nm whereas enhancement has been reported mostly for distances between $\sim$5 and 20 nm [79, 80]. Based on these results, most existing SEF demonstrations,

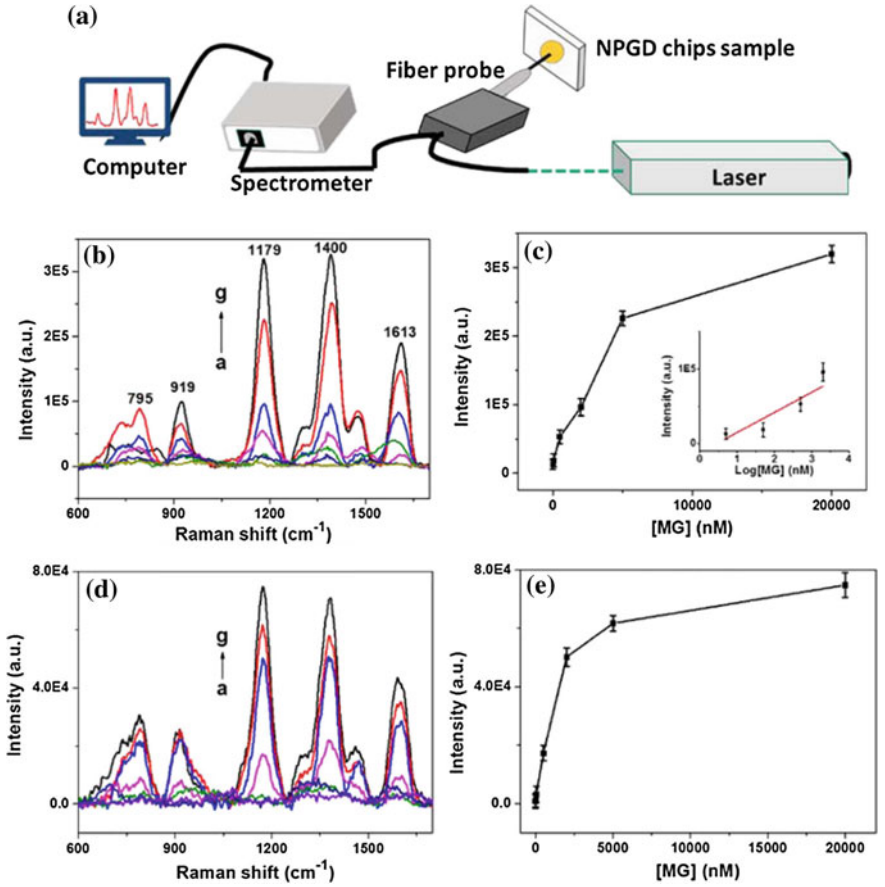

Fig. 27 **a** Portable Raman system with an optical fiber probe; **b** SERS spectra of various MG concentrations in PBS buffer solution; from a−g are 0 nM, 5 nM, 50 nM, 500 nM, 2 μM, 5 μM, and 20 μM, respectively; **c** plot of SERS intensity at 1179 cm^{-1} versus MG concentration, inset: linear range of SERS intensity at 1179 cm^{-1} versus MG concentration 5.nM−2 μM. **d** SERS spectra of fish samples spiked with various MG concentrations; from a−g are 0 nM, 5 nM, 50 nM, 500 nM, 2 μM, 5 μM, and 20 μM, respectively; **e** plot of SERS intensity at 1179 cm^{-1} versus MG concentration. Laser wavelength, 785 nm; acquisition time, 0.5 s; accumulation time, 30 s

including those on thin-film NPG materials, involve spacers to place fluorophores at the "ideal" distance from the metal [81, 82].

Here the label-free NPGD sensor is based on the scheme presented in Sect. 4.2 with a distance modulation scheme based on targeted DNA hybridization to a "hairpin" single-stranded DNA (ssDNA) probe featuring a Cyanine 3 (Cy3) fluorophore on the 3′-end and a sulfur on the 5′-end. The distance between the Cy3 molecule and NPGD can be altered. By taking advantage of the distance modulation, the sensitivity of the NPGD sensor to target DNA with 28 complementary

base pairs is demonstrated. The hairpin probe sequence which is employed is complementary to the ERBB2 gene, a target breast cancer DNA biomarker.

5.3.1 Fluorescence Enhancement on NPG Disks Arrays

Fluorescence emission spectra were acquired using home-built inverted fluorescence microscopy systems with 532 and 785 nm CW laser sources. 400 nm diameter NPG disks arrays on glass are fabricated according to the method described in Sect. 2 and the dyes rhodamine 6G (R6G, 526/560 nm), Cy3 (550/570 nm), and IRDye 800 (780/800 nm) are used to investigate the SEF properties of NPG disks, 400 nm Au disks, flat gold, and glass substrates.

For R6G concentration ranging from 100 nM to 1 μM, a net total fluorescence gain up to 50 is measured on NPGD versus fluorescence on glass substrate whereas for lower R6G concentrations, between 20 nM and 5 nM, quenching of fluorescence intensity is observed [74]. It is worth mentioning here that these values should not be interpreted as the SEF enhancement factor on NPGD because the total fluorescence signals are the outcome of combined quenching and enhancement effects which are likely affected by the average surface density of the adsorbed dye molecules.

To characterize the fluorescence enhancement properties of NPGDs, fluorescence emission spectra are collected from three dyes on three different gold substrates: the NPGDs are of 400 nm diameter, 75 nm thickness, and 13 nm average pore size, the non-porous gold disks are of the same external size and the flat gold film is 75 nm in thickness. All fluorescence spectra are normalized to the peak value of the one obtained from the glass substrate. The results are presented on Fig. 28.

NPGD substrates exhibit the strongest total fluorescence for all three dyes, as compared to the other gold substrates (gold disk and gold film). The net gain obtained on NPGD substrates is ~7, 7, and 1.75 times compared to the glass substrate for R6G, Cy3, and IRDye 800, respectively. The flat gold substrate

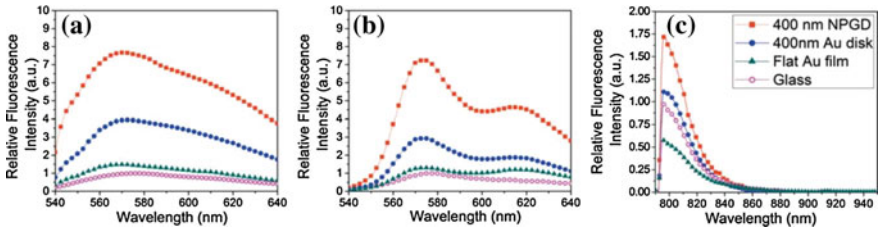

Fig. 28 Comparison of fluorescence spectra from 3 dyes on 4 substrates: **a** R6G and **b** Cy3 dyes dried on NPGD and gold disk samples acquired using a home-built fluorescence microscope with 532 nm excitation, **c** IRDye 800 dye fluorescence measured using a home-built fluorescence microscope with 785 nm excitation. An amount of 5 μL of the 100 nM aqueous dye solutions was drop-casted on each substrate

provides the lowest fluorescence with net gain slightly larger than 1 for R6G and Cy3, and ~0.6 for IRDye, suggesting quenching dominates over enhancement. The non-porous gold disks provide medium fluorescence with net gain ~3–4 times for R6G and Cy3, and 1.15 times for IRDye. The larger net gain on NPGDs is attributed to higher field enhancement within the high-density plasmonic hot spots, which are unique features only seen in NPGDs and this higher enhancement is measured despite the fact that the LSPR peak for the non-porous Au disks is closer to the excitation/emission wavelengths for either the visible or NIR dyes.

5.3.2 Zeptomole Detection of the ERBB2 Cancer DNA Biomarker

A "hairpin" ssDNA probe is employed to detect ERBB2 breast cancer biomarker. The probe features a Cy3 on the 3′-end and a sulfur on the 5′-end that enables effective binding to gold surfaces. If the probe alone is bonded, the Cy3 molecule is positioned at the close proximity of the NPGD surface, which promotes quenching. In contrast, a hybridized dsDNA would have the Cy3 molecule on the opposite end of the sulfur and far away from the NPGD surface after binding. As compared to the un-hybridized hairpin probe on NPGD, higher fluorescence intensity is expected for the dsDNA configuration, providing an effective sensing mechanism. (See Fig. 29) In the previous drop casting method, the likelihood for the fluorophore molecules to be situated in the enhancing hot spots of the NPGD is highly dependent on the local dye-NPGD molecular interactions and dye concentration. In contrast, due to its inherent self-assembly mechanism and robust sulfur-gold covalent binding, the thiolated probe structure ensures a uniform molecular coverage on the gold surface. These features of the hairpin probe minimize the randomness of its molecular attachment to the NPGD substrate and, thus, increases the precision of molecular coverage on the three-dimensional structure of NPGDs.

In Fig. 30, the total Cy3 fluorescence intensity dependence on ssDNA target sequence concentration is presented. Different amounts (0–5 μL) of the ssDNA

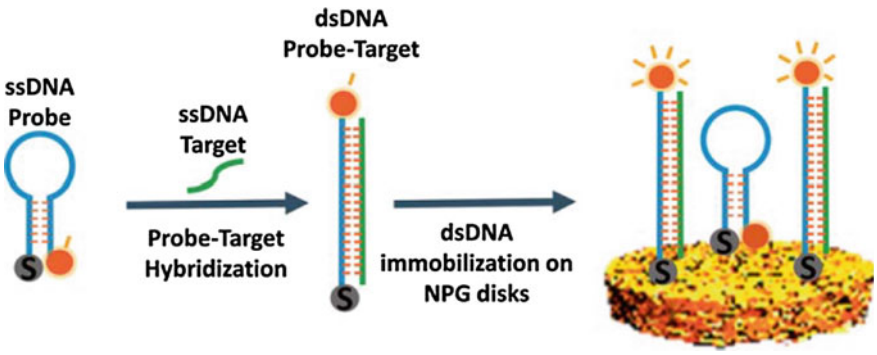

Fig. 29 Schematic of the hairpin probe and probe-target (dsDNA) configurations of the ERBB2 cancer gene, and their immobilization on NPGDs

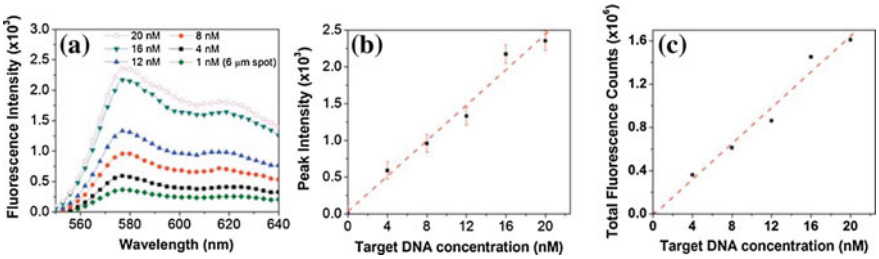

Fig. 30 Fluorescence spectra, peak intensity and total fluorescence counts: **a** with the probe signal used as reference baseline, the difference spectra at different target DNA concentration are plotted as labeled. Corresponding **b** peak intensity and **c** total intensity counts for each concentration step of the target DNA

target sequence (40 nM) are mixed and hybridized with a fixed amount of the hairpin probe (5 μL, 40 nM) at 50 °C for 60 min. With added phosphate buffer solution to a total 10 μL volume, different final concentrations of hybridized dsDNA and non-hybridized probe molecules are obtained. After cooling, 5 μL of each sample is dispensed onto the NPGD substrate surrounded by a PDMS well (2 mm diameter, 4 mm height) and allowed to incubate for 60 min. The surface is then washed with deionized (DI) water and incubated in 0.1 mM mercapto-1-hexanol (MCH) for 30 min to eliminate nonspecific binding, followed by DI water rinse. In Fig. 30, the difference spectra are shown by subtracting the baseline spectrum (0 nM target) from others. At 4 nM target concentration, the amount of dsDNA molecules is estimated to be $\sim$2.4 zeptomole with a signal-to-noise ratio (SNR) of $\sim$123 based on the laser spot size and the surface density calculation. In principle, based on the signal-to-noise ratio, the ultimate limit of detection (LOD) in quantity would be $\sim$0.06 zeptomole for SNR $\sim$3.

Next, the LOD in concentration depends on the measurement spot size. At any fixed target molecules concentration, more fluorescence can be acquired from a larger spot with more molecules. Therefore, lower concentration LOD beyond 4 nM can be achieved. Since we are only measuring the ensemble average of the enhanced population over the laser spot, the detection limit can be only be estimated according to the expected coverage at a given target concentration; the statistical limitation of the signal averaging of the enhanced molecules deters single-molecule detection.

6 Conclusion

Continual scientific discoveries and technological advances in nanoplasmonic over the past two decades have stimulated exciting development of biosensing assays and platforms. The pursuit of measuring trace analytes and biomolecules from a tiny sample volume has driven the field towards high surface-to-volume ratio

metallic nanostructures. This is of particular interest to the fields of medical diagnostics, environmental toxin detection, and molecular biology. On one hand, the ability to detect trace disease biomarker at unprecedentedly low concentration can lead to early detection of various diseases such as cancer where the best treatment is early detection. On the other hand, many environmental trace toxins, although do not pose imminent health threat, can have profound negative impact after prolonged exposure and accumulation in biological subjects. Therefore, successful detection at the low concentration can be extremely important. In addition, nanoplasmonic sensing either by refractive index changes or enhanced light–matter interactions can often be implemented in a label-free fashion where the target analytes are in their most original form. Furthermore, the ability to test small volume is a practical advantage for clinical and other applications where sample collection is costly. It is therefore desirable to focus our current efforts on the design of reliable, robust, and low-cost nano-biosensors which can be integrated efficiently into routine laboratory as well as point-of-care testing and environmental monitoring. The central subject of this chapter deals with recent advances in the science and technology of nanoporous gold nanoparticles and arrays with a particular emphasis on their biosensing applications enabled by the unique combinations of large surface-to-volume ratio, three-dimensional high-density hot spots, and architectural integrity and compatibility with other planar fabrication processes.

NPG disks are easy to fabricate, low-cost and very versatile. Their three-dimensional porous network yields a unique surface-to-volume ratio and multiplies the sensing sites that analytes can reach. Their high plasmonic tunability enables one to tailor them to specific needs by changing their interior and exterior morphology. Varying their diameter is achieved straightforwardly thanks to their top-down nano-patterning and the porosity can be modified through thermal or chemical post-treatment. NPG disks can be furthermore monolithically integrated into a microfluidic device and undergo surface modifications to increase their sensing specificity.

Several label-free nanobiosensing examples discussed in the chapter can be classified into two groups: with or without advanced surface functionalization. In the former, we have shown that ultrahigh sensitivity can be achieved in sequence-specific DNA hybridization monitoring at the single-molecule level using molecular sentinel, and direct sensing of small molecules such as malachite green using G-quadruplex as a capturing scaffold. Using advanced surface functionalization greatly improves sensitivity and specificity at the price of limited multiplexing. In the latter, we have demonstrated that bare-surfaced NPG disks can successfully quantify key analytes in unprocessed biological fluids such as urine, with the potential of highly multiplexed assays. We believe that nanoplasmonic biosensing based on NPG nanoparticles and arrays has exciting exciting commercialization potential for biomedical diagnostics and environmental monitoring applications.

References

1. Dror S, William C (2010) Modern introduction to surface plasmons. Cambridge University Press, Cambridge, UK
2. Zia R, Schuller SA, Chandran A, Brongersma ML (2006) Plasmonics: the next chip-scale technology. Mater Today 9(7–8):20–27
3. Polman A, Atwater HA (2005) Plasmonics: optics at the nanoscale. Mater Today 8:56
4. Lal S, Link S, Halas NJ (2007) Nano-optics from sensing to waveguiding. Nat Photonics 11(11):641–648
5. Tokel O, Inci F, Demirci U (2014) Advances in plasmonic technologies for point of care applications. Chem Rev 114(11):5728–5752
6. Vo-Dinh T, Fales AM, Griffin GD, Khoury CG, Liu Y, Ngo H, Norton SJ, Register JK, Wang H-N, Yuan H (2013) Plasmonic nanoprobes: from chemical sensing to medical diagnostics and therapy. Nanoscale 5:10127–10140
7. Sotiriou GA (2013) Biomedical applications of multifunctional plasmonic nanoparticles. WIREs Nanomedicine Nanobiotechnoly 5:19–30
8. Shih W-C, Santos GM, Zhao F, Zenasni O, Arnob MMP (2016) Simultaneous chemical and refractive index sensing in the 1−2.5 μm near-infrared wavelength range on nanoporous gold disks. Nano Lett 16:4641–4647
9. Le Ru E, Etchegoin P (2008) Principles of Surface-Enhanced Raman Spectroscopy and related plasmonic effects. Elsevier
10. Brolo AG (2012) Plasmonics for future biosensors. Nat Photonics 6(11):709–713
11. Pitsillides CM, Joe EK, Wei X, Anderson RR, Lin CP (2003) Selective cell targeting with light-absorbing microparticles and nanoparticles. Biophys J 84:4023–4032
12. Huang X, Jain PK, El-Sayed IH, El-Sayed MA (2006) Determination of the minimum temperature required for selective photothermal destruction of cancer cells with the use of immunotargeted gold nanoparticles. Photochem Photobiol 82(2):412–417
13. Hirsch LR, Stafford JR, Bankson JA, Sershen SR, Rivera B, Price R, Hazle JD, Halas NJ, West JL (2003) Nanoshell-mediated near-infrared thermal therapy of tumors under magnetic resonance guidance. Proc Natl Acad Sci 100(23):13549–13554
14. Loo C, Lowery A, Halas N, West J, Drezek R (2005) Immunotargeted nanoshells for integrated cancer imaging and therapy. Nano Lett 5(4):709–711
15. Biener J, Nyce GW, Hodge AM, Biener MM, Hamza AV, Maier SA (2008) Nanoporous plasmonic metamaterials. Adv Mater 20(6):1211–1217
16. Lang X, Qian L, Guan P, Zi J, Chen M (2011) Localized surface plasmon resonances of nanoporous gold. Appl Phys Lett 98(9):093701
17. Liu H, Zhang L, Lang X, Yamaguchi Y, Iwasaki H, Inouye Y, Xue Q, Chen M (2011) Single molecule detection from a large-scale SERS-active $Au_{79}Ag_{21}$ substrate. Sci Rep 1:112
18. Qi J, Motwani P, Gheewala M, Brennan C, Wolfe JC, Shih W-C (2013) Surface-enhanced Raman spectroscopy with monolithic nanoporous gold disk substrates. Nanoscale 5(10): 4105–4109
19. Ruan W-D, Lu Z-C, Ji N, Wang C-X, Bing Z, Zhang J-H (2007) Facile fabrication of large area polystyrene colloidal crystal monolayer via surfactant-free Langmuir-Blodgett technique. Chem Res Chin Univ 23(6):712–714
20. Parida S, Kramer D, Volkert CA, Rosner H, Erlebacher J, Weissmuller J (2006) Volume change during the formation of nanoporous gold by dealloying. Phys Rev Lett 97(3):035504
21. Crowson DA, Farkas D, Corcoran SG (2007) Geometric relaxation of nanoporous metals: the role of surface relaxation. Scr mater 56(11):919–922
22. Read JS (1988) Introduction to the principle of ceramic processing. Wiley
23. Seker E, Berdichevsky Y, Begley MR, Reed ML, Staley KJ, Yarmush ML (2010) The fabrication of low-impedance nanoporous gold multiple-electrode arrays for neuralelectrophysiology studies. Nanotechnology 21(12):125504

24. Zhao F, Zeng J, Santos GM, Shih W-C (2015) In situ patterning of hierarchical nanoporous gold structures by in-plane dealloying. Mater Sci Eng B 194:34–40
25. Li J, Zhao F, Shih W-C (2016) Direct-write patterning of nanoporous gold microstructures by in situ laser-assisted dealloying. Opt Express 24(20):23610–23617
26. Qian L, Chen M (2007) Ultrafine nanoporous gold by low-temperature dealloying and kinetics of nanopore formation. Appl Phys Lett 91(8):083105
27. Strehle KR, Cialla D, Rosch P, Henkel T, Kohler M, Popp J (2007) A reproducible surface-enhanced Raman spectroscopy approach. Online SERS measurements in a segmented microfluidic system. Anal Chem 79(4):1542–1547
28. Quang LX, Lim C, Seong GH, Choo J, Do KJ, Yoo S-K (2008) A portable surface-enhanced Raman scattering sensor integrated with a lab-on-a-chip for field analysis. Lab Chip 8(12): 2214–2219
29. Sun J, Xianyu Y, Jiang X (2014) Point-of-care biochemical assays using gold nanoparticle-implemented microfluidics. Chem Soc Rev 43(17):6239–6253
30. Dee KC, Puleo DA, Bizios R (2003) An introduction to tissue-biomaterial interactions. Wiley
31. Santos GM, Zhao F, Zeng J, Shih W-C (2014) Characterization of nanoporous gold disks for photothermal light harvesting and light-gated molecular release. Nanoscale 6(11):5718–5724
32. Qi J, Zeng J, Zhao F, Lin SH, Raja B, Strych U, Willson RC, Shih W-C (2014) Label-free, in situ SERS monitoring of individual DNA hybridization in microfluidics. Nanoscale 6(15):8521–8526
33. Li M, Zhao F, Zeng J, Qi J, Lu J, Shih W-C (2014) Microfluidic surface-enhanced Raman scattering sensor with monolithically integrated nanoporous gold disk arrays for rapid and label-free biomolecular detection. J Biomed Opt 19(11):111611
34. Li M, Li S, Cao W, Li W, Wen W, Alici G (2012) Continuous particle focusing in a waved microchannel using negative DC dielectrophoresis. J Micromech Microeng 22(9):095001
35. Ding Y, Chen M (2009) Nanoporous metals for catalytic and optical applications. MRS Bull 34(08):569–576
36. Yu F, Ahl S, Caminade A-M, Majoral J-P, Knoll W, Erlebacher J (2006) SPP and LSPR in NPG membranes. Anal Chem 78(20):7346–7350
37. Wittstock A, Biener J, Erlebacher J (2012) Nanoporous gold: from an ancient technology to a high-tech material. R Soc Chem
38. Ryckman JD, Jiao Y, Weiss SM (2013) Three-dimensional patterning and morphological control of porous nanomaterials by gray-scale direct imprinting. Sci Rep 3
39. Halas NJ, Lal S, Link S, Chang W-S, Natelson D, Hafner JH, Nordlander P (2012) A plethora of plasmonics from the laboratory for nanophotonics at Rice University. Adv Mater 24(36): 4842–4877
40. Zeng J, Zhao F, Qi J, Li Y, Li C-H, Yao Y, Lee RT, Shih W-C (2014) Internal and external morphology-dependent plasmonic resonance in monolithic nanoporous gold nanoparticles. RSC Adv 4(69):3688–36682
41. Zhao F, Zeng J, Arnob MMP, Sun P, Qi J, Motwani P, Gheewala M, Li C-H, Paterson A, Strych U, Raja B, Willson RC, Wolfe JC, Lee TR, Shih W-C (2014) Monolithic NPG nanoparticles with large surface area, tunable plasmonics and high-density internal hot spots. Nanoscale 6(14):8199–8207
42. Camden JP, Dieringer JA, Zhao J, Van Duyne RP (2008) Controlled plasmonic nanostructures for surface-enhanced spectroscopy and sensing. Acc Chem Res 41(12):1653–1661
43. Kucheyev SO, Hayes JR, Biener J, Huser T, Talley CE, Hamza AV (2006) Surface-enhanced Raman scattering on nanoporous Au. Appl Phys Lett 89(5):053102
44. Gloria D, Gooding JJ, Moran G, Hibbert BD (2011) Electrochemically fabricated three dimensional nano-porous gold films optimised for surface enhanced Raman scattering. J Electroanal Chem 656(1):114–119
45. Li Z, Yang Y, Xia Y, Huang W, Zheng J, Li Z (2012) Fabrication of nano-network gold films via anodization of gold electrode and their application in SERS. J Solid State Electrochem 16(4):1733–1739

46. Aggarwal RL, Farrar LW, Diebold ED, Polla DL (2009) Measurement of the absolute Raman scattering cross section of the 1584-cm^{-1} band of benzenethiol and the surface-enhanced Raman scattering cross section enhancement factor for femtosecond laser-nanostructured substrates. J Raman Spectrosc 40(9):1331–1333
47. Gui JY, Stern DA, Frank DG, Lu F, Zapien DC, Hubbard AT (1991) Adsorption and surface structural chemistry of thiophenol, benzyl mercaptan, and alkyl mercaptans. Comparative studies at silver (111) and platinum (111) electrodes by means of Auger spectroscopy, electron energy loss spectroscopy, low energy electron dif. Langmuir 7(5):955–963
48. Jiao Y, Ryckman JD, Ciesielski PN, Escobar CA, Jennings KG, Weiss SM (2011) Patterned nanoporous gold as an effective SERS template. Nanotechnology 22(29):295302
49. Sun Y, Xia Y (2002) Increased sensitivity of surface plasmon resonance of gold nanoshells compared to that of gold solid colloids in response to environmental changes. Analitycal Chem 74(20):5297–5305
50. Hanarp P, Käll M, Sutherland DS (2003) Optical properties of short range ordered arrays of nanometer gold disks prepared by colloidal lithography. J Phys Chem B 107(24):5768–5772
51. Hu M, Chen J, Marquez M, Xia Y, Hartland GV (2007) Correlated rayleigh scattering spectroscopy and scanning electron microscopy studies of Au-Ag bimetallic nanoboxes and nanocages. J Phys Chem C 111(34):12558–12565
52. Jain PK, Huang X, El-Sayed IH, El-Sayed MA (2008) Noble metals on the nanoscale: optical and photothermal properties and some applications in imaging, sensing, biology, and medicine. Acc Chem Res 41(12):1578–1586
53. Wang H, Brandl DW, Le F, Nordlander P, Halas NJ (2006) Nanorice: a hybrid plasmonic. Nano Lett 6(4):827–832
54. Larsson EM, Alegret J, Käll M, Sutherland DS (2007) Sensing characteristics of NIR localized surface plasmon resonances in gold nanorings for application as ultrasensitive biosensors. Nano Lett 7(5):1256–1263
55. Qi J, Shih W-C (2012) Parallel Raman microspectroscopy using programmable multipoint illumination. Opt Lett 37(8):1289–1291
56. Park SG, Lee NS, Lee SH (2000) Vibrational analysis of dopamine neutral Bae based on density functional force field. Bull Korean Chem Soc 21(10):1035–1038
57. Sassolas A, Leca-Bouvier BD, Blum LJ (2008) DNA biosensors and microarrays. Chem Rev 108(1):109–139
58. Lu Y, Liu GL, Kim J, Mejia YX, Lee LP (2005) Nanophotonic crescent moon structures with sharp edge for ultrasensitive biomolecular detection by local electromagnetic field enhancement effect. Nano Lett 5(1):119–124
59. Kang T, Yoo SM, Yoon I, Lee SY, Kim B (2010) Patterned multiplex pathogen DNA detection by Au particle-on-wire SERS sensor. Nano Lett 10(4):1189–1193
60. Wang H-N, Dhawan A, Du Y, Batchelor D, Leonard DN, Misra V, Vo-Dinh T (2013) Molecular sentinel-on-chip for SERS-based biosensing. Phys Chem Chem Phys 15(16):6008–6015
61. Wang H-N, Fales AM, Zaas AK, Woods CW, Burke T, Ginsburg GS, Vo-Dinh T (2013) Surface-enhanced Raman scattering molecular sentinel nanoprobes for viral infection diagnostics. Anal Chim Acta 786:153–158
62. Cao YC, Jin R, Mirkin CA (2002) Nanoparticles with Raman spectroscopic fingerprints for DNA and RNA detection. Science 297(5586):1536–1540
63. Shih WC (2014) Label-free in situ SERS monitoring of individual DNA hybridization in microfluidics. Nanoscale 6(5):8521–8526
64. Li M, Lu J, Qi J, Zhao F, Zeng J, Yu JC-C, Shih W-C (2014) Stamping surface-enhanced Raman spectroscopy for label-free, multiplexed, molecular sensing and imaging. J Biomed Opt 19(5):050501
65. Li M, Du Y, Zhao F, Zeng J, Mohan C, Shih W-C (2015) Reagent-and separation-free measurements of urine creatinine concentration using stamping surface enhanced Raman scattering (S-SERS). Biomed Opt Express 6(3):849–858

66. Xie C, Sharma R, Wang H, Zhou XJ, Mohan C (2004) Strain distribution pattern of susceptibility to immune-mediated nephritis. J Immunol 172(8):5047–5055
67. Qiu S, Zhao F, Zenasni O, Li J, Shih W-C (2016) Nanoporous gold disks functionalized with stabilized G-quadruplex moieties for sensing small molecules ACS Appl Mater Interfaces 8(44):29968–29976
68. Bhasikuttan AC, Mohanty J (2015) Targeting G-quadruplex structures with extrinsic fluorogenic dyes: promising fluorescence sensors. Chem Commun 51(36):7581–7597
69. Biffi G, Di Antonio M, Tannahill D, Balasubramanian S (2014) Visualization and selective chemical targeting of RNA G-quadruplex structures in the cytoplasm of human cells. Nat Chem 6(1):75–80
70. Olejko L, Cywinski PJ, Bald I (2015) Ion-Selective formation of a guanine quadruplex on DNA origami structures. Angew Chem Int Ed 54(2):673–677
71. Koirala D, Dhakal S, Ashbridge B, Sannohe Y, Rodriguez R, Sugiyama H, Balasubramanian S, Mao H (2011) A single-molecule platform for investigation of interactions between G-quadruplexes and small-molecule ligands. Nat Chem 3(10):782–787
72. Bhasikuttan AC, Mohanty J, Pal H (2007) Interaction of malachite green with guanine-rich single-stranded DNA: preferential binding to a G-Quadruplex. Angew Chem Int Ed 46(48): 9305–9307
73. Srivastava S, Sinha R, Roy D (2004) Toxicological effects of malachite green. Aquat Toxicol 66(3):319–329
74. Santos GM, Zhao F, Zeng J (2015) Label-free, zeptomole cancer biomarker detection by surface-enhanced fluorescence on nanoporous gold disk plasmonic nanoparticles. J Biophotonics 8(10):855–863
75. Geddes CD, Parfenov A, Roll D, Gryczynski I, Malicka J, Lakowicz JR (2003) Silver fractal-like structures for metal-enhanced fluorescence: enhanced fluorescence intensities and increased probe photostabilities. J Fluoresc 13(3):267–276
76. Gartia MR, Hsiao A, Sivaguru M, Chen Y, Liu LG (2011) Enhanced 3D fluorescence live cell imaging on nanoplasmonic substrate. Nanotechnology 22(36):365203
77. Chen Y, Munechika K, Ginger DS (2007) Dependence of fluorescence intensity on the spectral overlap between fluorophores and plasmon resonant single silver nanoparticles. Nano Lett 7(3):690–696
78. Ranjan Gartia M, Eichorst JP, Clegg RM, Logan Liu G (2012) Lifetime imaging of radiative and non-radiative fluorescence decays on nanoplasmonic surface. Appl Phys Lett 101 (2):023118
79. Anger P, Bharadwaj P, Novotny L (2006) Enhancement and quenching of single-molecule fluorescence. Phys Rev Lett 96(11):113002
80. Campion A, Gallo AR, Harris CB, Robota HJ, Whitmore PM (1980) Electronic energy transfer to metal surfaces: a test of classical image dipole theory at short distances. Chem Phys Lett 73(3):447–450
81. Lang XY, Guan PF, Fujita T, Chen M (2011) Tailored nanoporous gold for ultrahigh fluorescence enhancement. Phys Chem Chem Phys 13(9):3795–3799
82. Lang XY, Guan PF, Zhang L, Fujita T, Chen M (2010) Size dependence of molecular fluorescence enhancement of nanoporous gold. Appl Phys Lett 96(7):073701